Titre: Title:	Paper-Based Microfluidic Devices for Paper Spray Mass Spectrometry Analysis
Auteur: Author:	Linda Taam
Date:	2025
Type:	Mémoire ou thèse / Dissertation or Thesis
Référence: Citation:	Taam, L. (2025). Paper-Based Microfluidic Devices for Paper Spray Mass Spectrometry Analysis [Master's thesis, Polytechnique Montréal]. PolyPublie. https://publications.polymtl.ca/67682/

POLYTECHNIQUE MONTRÉAL
affiliée à l'Université de Montréal

Paper-Based Microfluidic Devices for Paper Spray Mass Spectrometry Analysis

LINDA TAAM
Institut de génie biomédical

Mémoire présenté en vue de l'obtention du diplôme de *Maîtrise ès sciences appliquées*

Génie biomédical

Août 2025

POLYTECHNIQUE MONTRÉAL
affiliée à l'Université de Montréal

Ce mémoire intitulé :

Paper-Based Microfluidic Devices for Paper Spray Mass Spectrometry Analysis

présenté par **Linda TAAM**
en vue de l'obtention du diplôme de *Maîtrise ès sciences appliquées*
a été dûment accepté par le jury d'examen constitué de :

Fabio CICOIRA, président
Raphaël TROUILLON, membre et directeur de recherche
Melissa K. PASSARELLI, membre et codirectrice de recherche
Lucien WEISS, membre

DEDICATION

To my family for their support.

ACKNOWLEDGEMENTS

I would like to express my sincere gratitude to my research supervisor, Professor Raphaël Trouillon, for his guidance, support, and patience throughout this project. His expertise and thoughtful advice have been instrumental in the development and completion of this thesis.

I also wish to thank my co-supervisor, Professor Melissa Passarelli, for her valuable insights and contributions, which have helped shape the direction and depth of this research.

I am grateful to my colleagues and all members of the laboratory at Polytechnique Montréal for their support, insightful discussions, and the collaborative atmosphere they helped foster. I would like to especially acknowledge Sabrina Zoso, whose prior work provided a solid foundation for this project and greatly facilitated its continuation.

My thanks also go to the members of the laboratory at Concordia University, particularly Adam Bouguila and Jingsuy Sun, for their technical assistance and generous support during key stages of this research.

Finally, I would like to extend my heartfelt thanks to my friends and family for their constant encouragement and presence throughout this journey. I am especially grateful to my sister, Amina Taam, whose unwavering support, kindness, and motivation have meant a great deal to me. Her presence has been a true source of strength and reassurance along the way.

RÉSUMÉ

La spectrométrie de masse par pulvérisation sur papier reste une technique encore peu explorée, malgré son fort potentiel analytique, en particulier pour l'étude des biomolécules. Dans ce travail, nous présentons une caractérisation de cette technique à l'aide d'un dispositif microfluidique sur papier développé au sein de notre laboratoire, dans le but de mieux comprendre les mécanismes fondamentaux régissant la génération d'ions multiprotonés de protéines, en prenant la myoglobine comme analyte modèle. Plus spécifiquement, notre étude examine l'influence de la géométrie de la pointe, de la microstructure du papier ainsi que des propriétés physico-chimiques du couple solvant–substrat sur l'efficacité d'ionisation et sur la distribution des états de charge.

La méthodologie adoptée repose sur trois approches complémentaires. Les observations en microscopie électronique environnementale ont mis en évidence des réseaux de pores hétérogènes ainsi que des irrégularités liées à la technique de découpe laser, confirmant la variabilité intrinsèque des propriétés de surface. Des simulations numériques réalisées sous COMSOL Multiphysics ont permis de cartographier le champ électrostatique au voisinage de la pointe. Les résultats indiquent que des pointes plus aiguës (15°) génèrent un champ plus intense et plus localisé que des pointes à angle plus élevé (30° et 45°), favorisant ainsi une zone d'ionisation plus confinée. En parallèle, des expériences de spectrométrie de masse par pulvérisation sur papier ont été réalisées sur la myoglobine, en faisant varier plusieurs paramètres : l'angle de la pointe, le débit du solvant par rapport au substrat et le pH du solvant. Les spectres de masse obtenus montrent que la diminution du pH déplace systématiquement la distribution des états de charge vers des valeurs plus élevées, ce qui montre que la puce microfluodique est capable de détecter les différentes conformations de la myoglobine (compacte ou allongée). Les résultats montrent que l'efficacité d'ionisation et la distribution des états de charge dépendent fortement des conditions de solution et des propriétés du papier. À pH élevé, de grosses gouttelettes et un débit élevé favorisent l'ionisation, tandis qu'à pH faible, de petites gouttelettes et un débit réduit induisent plusieurs états de protonation. La taille des pores et le débit, paramètres interdépendants, doivent être considérés conjointement pour optimiser l'angle de la pointe.

Ce travail montre que la puce élaborée assure une détection protéique fiable par PS-MS et constitue une plateforme pour optimiser rationnellement les μPADs, ouvrant la voie à des performances accrues et à de nouvelles applications analytiques.

ABSTRACT

This work investigates the performance and underlying mechanisms of PS-MS using a custom-designed μPAD fabricated in our laboratory. The objectives were to validate its analytical reliability for protein detection, to examine how the physical and chemical properties of paper substrates influence ionization, and to gain a deeper understanding of the processes governing droplet formation and charge generation. Myoglobin was selected as a model protein to assess the efficiency and stability of ionization under controlled experimental conditions. The device yielded reproducible mass spectra with well-defined charge-state distributions, demonstrating its potential as a reliable platform for protein detection.

The intrinsic microstructural properties of the paper were characterized using an ESEM, revealing edge irregularities introduced by laser cutting. These observations highlighted the inherent randomness of paper at the microscale and its potential impact on fluid transport and ionization. Numerical simulations performed in the COMSOL Multiphysics software provided additional insight into the electrostatic field near the paper tip. Tip geometry was shown to play a critical role: narrower angles produced more confined and intense electric fields, promoting localized ionization at high flow rates. Furthermore, spectral analysis showed that, at low pH, smaller pore sizes and reduced flow rates produced finer droplets, improving desolvation and broadening the charge state distribution. Pore size and solvent flow rate emerged as interdependent factors that determine the optimal tip angle. At higher pH, larger pore sizes enhanced ionization efficiency, although this effect was modulated by the flow rate. Overall, lowering the solution pH consistently shifted the charge state distributions toward higher charge states, in agreement with the different conformations taken by the myoglobin.

These results, combined with the electrostatic modeling, indicate that ionization efficiency is jointly controlled by substrate microstructure, tip geometry, and solution chemistry. Although the device demonstrated stable and reproducible protein ionization and provided valuable insights into the physicochemical factors affecting PS-MS, limitations remain, including structural variability due to laser cutting. Future work should focus on improving substrate fabrication, extending modeling simulations, and enhancing geometric control to further increase reproducibility and analytical performance.

Overall, this study confirms that μPADs can be effectively adapted for stable PS-MS protein analysis while also serving as powerful experimental platforms for probing how material heterogeneity and operational parameters shape ionization mechanisms.

TABLE OF CONTENTS

LIST OF TABLES

LIST OF FIGURES

LIST OF SYMBOLS AND ACRONYMS

AIMS	Ambient Ionization Mass Spectrometry
APCI	Atmospheric Pressure Chemical Ionization
API	Atmospheric Pressure Ionization
CBAMS	Concordia Center for Biological Applications of Mass Spectrometry
CEM	Charge Ejection Model
CRM	Charge Residue Model
DART	Direct Analysis in Real Time
DESI	Desorption Electrospray Ionization
DNA	Deoxyribonucleic Acid
EI	Electron Impact
ELISA	Enzyme-Linked Immunosorbent Assay
ESEM	Environmental Scanning Electron Microscope
ESI	Electrospray Ionization
GC-MS	Gas Chromatography–Mass Spectrometry
LC-MS	Liquid Chromatography–Mass Spectrometry
LOQ	Limit of Quantification
MALDI	Matrix-Assisted Laser Desorption/Ionization
MGF	Mesoporous Graphene Foam
MS	Mass Spectrometry
NMR	Nuclear Magnetic Resonance
POC	Point Of Care
PSI	Paper Spray Ionization
PS-MS	Paper Spray–Mass Spectrometry
RNA	Ribonucleic Acid
SIMS	Secondary Ion Mass Spectrometry
μPAD	Microfluidic Paper-based Analytical Device
SD	Standard Deviation

LIST OF APPENDICES

CHAPTER 1 INTRODUCTION

In recent years, advances in analytical technologies have significantly enhanced the sensitivity and precision of biomolecular detection, enabling a deeper understanding of complex biological systems [12]. Among these technologies, mass spectrometry (MS) has emerged as a key tool in biomedical analysis due to its high sensitivity and specificity. The development of ambient ionization techniques has further expanded the capabilities of MS by allowing rapid analysis with minimal sample preparation, paving the way for point-of-care (POC) applications.

However, conventional methods such as liquid chromatography–mass spectrometry (LC-MS), gas chromatography–mass spectrometry (GC-MS), nuclear magnetic resonance (NMR), and enzyme-linked immunosorbent assay (ELISA) often involve complex workflows, expensive instrumentation, or are restricted to predefined targets. These limitations underline the growing need for analytical strategies that are fast, simple, robust, cost-effective, and user-friendly [12].

In this context, a novel technique known as paper spray mass spectrometry (PS-MS) was introduced in 2010 by Liu *et al.* as a promising alternative analytical method [13]. It enables the direct analysis of untreated biofluids with minimal preparation, using a simple piece of paper as both the sampling medium and ionization surface electrode. PS-MS has demonstrated broad applicability in the detection of drugs, metabolites, lipids, and proteins [14].

Despite its potential, PS-MS remains insufficiently explored and lacks standardization. Key parameters—such as paper type, device geometry, solvent composition, and ionization mechanisms—still require systematic optimization, as they directly impact signal intensity, stability, and reproducibility. The performance of PS-MS is also highly dependent on the sample matrix and analyte. Protein analysis, in particular, remains challenging due to low ionization efficiency and surface interactions [15]. While notable progress has been made, further refinement and a deeper understanding of PS-MS fundamentals are essential to ensure its reliable use in both research and clinical applications [10].

Our objective is to characterize spray efficiency in PS-MS by examining the influence of critical parameters such as solvent composition, device geometry, and paper substrate type, using a custom-designed microfluidic paper device. This investigation aims to deepen our understanding of the fundamental mechanisms that govern ion generation and spray stability. To support this study, we employ myoglobin as a model analyte, owing to its well-defined structure and its frequent use as a reference protein in PS-MS research [15].

CHAPTER 2 LITERATURE REVIEW

2.1 Fundamentals of MS

MS is a powerful analytical technique known for its high sensitivity and specificity, capable of detecting and identifying compounds even at trace levels. It is widely applied in fields such as environmental monitoring, pharmaceutical research, clinical diagnostics, forensic science, and food safety [16, 17].

The fundamental principle of MS lies in measuring the mass-to-charge ratio (m/z) of ionized molecules, where m is expressed in daltons (Da). This allows for the identification and quantification of chemical compounds in both biological and non-biological samples. In a typical workflow, analytes are ionized, separated based on their m/z, and then detected. Beyond quantification, MS also provides structural and qualitative information, making it an essential tool in modern analytical chemistry.

2.1.1 MS mechanism

The MS process involves three essential steps:

- **Ionization of sample molecules:** Molecules in liquid or solid form are first converted into gas-phase ions using ionization techniques. This transformation is essential because only charged species can be accelerated, separated, and detected by the mass spectrometer. The efficiency and mechanism of ionization play a critical role in determining the method's sensitivity and the range of analytes that can be effectively detected.

- **Separation of ions by m/z ratio:** After ionization, the ions are accelerated by an electric potential, which gives them kinetic energy. All ions with the same charge receive approximately the same amount of energy. These ions are then directed into a Mass Analyzer—such as a quadrupole, Time-of-Flight (TOF), ion trap, or Orbitrap—where they are separated based on their mass-to-charge ratio (m/z). The analyzer type determines how well the instrument can distinguish between ions with very similar masses up to $\Delta m/m \sim 0.0004$ for an Orbitrap [17].

- **Detection and spectrum generation:** After separation, the ions reach the detector, where each ion generates an electrical signal proportional to its abundance. These

signals are then processed by a computer to create a mass spectrum—a graph that displays the intensity of detected ions as a function of their mass-to-charge ratio (m/z). This spectrum serves as a molecular fingerprint, providing information on the quantity of each ion generated and/or how larges molecules are fragmented, which helps in identifying and characterizing the compounds present in the sample.

As illustrated in Figure 2.1, the mass spectrometer produces a spectrum where each peak corresponds to a molecule ionized and detected in the sample for different levels of ionization. The **x-axis** indicates the mass-to-charge ratio (m/z), while the **y-axis** reflects the relative intensity, representing the abundance of each ion.

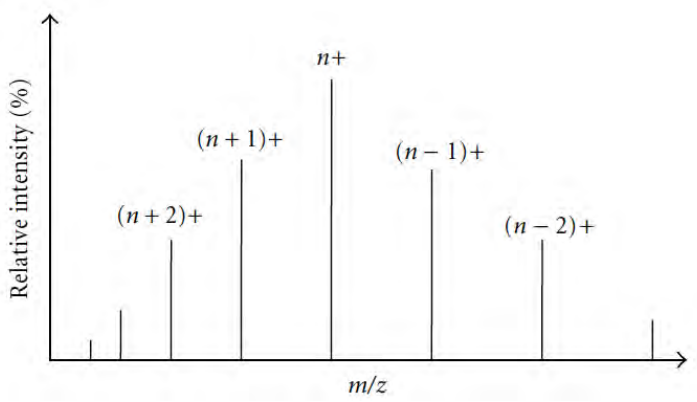

Figure 2.1 Schematic illustration of positively charged ion species [6], where n represent the charge state. Reproduced under the terms of the CC BY 3.0 license.

This spectrum acts as a molecular fingerprint, enabling:

- **Identification** of compounds via m/z values or fragmentation patterns,
- **Quantification** based on peak intensity,
- **Detection** of structural variants or impurities.

Thanks to continuous advancements in ionization sources, mass analyzers, and data processing technologies, MS has established itself as a gold standard in biomedical analysis, enabling sensitive and quantitative detection of biomolecules (proteins, peptides, oligosaccharides, lipids, Deoxyribonucleic Acid (DNA), and Ribonucleic Acid (RNA), drugs, and metabolites [18]).

As ionization is critical in MS, the choice of technique depends on the sample's volatility, polarity, and molecular weight. Analytes are converted into cations, anions, or adducts depending on the solvent, substrate, and detection mode (positive or negative, corresponding to the applied voltage polarity). The ionization energy directly influences the extent of fragmentation and, ultimately, the quality of the resulting mass spectrum. Several ionization methods are used in MS, including Electron Impact (EI) for small volatile compounds, Atmospheric Pressure Ionization (API) techniques like Electrospray Ionization (ESI) and Atmospheric Pressure Chemical Ionization (APCI), Secondary Ionization Mass Spectrometry (SIMS) as well as Matrix-Assisted Laser Desorption/Ionization (MALDI) for larger biomolecules such as proteins and peptides. Among these, our focus will be on ESI, an ambient ionization technique particularly well-suited for the direct analysis of biomolecules from complex matrices [17].

2.1.2 Electrospray Ionization : A key ambient ionization technique in MS

Ambient ionization techniques enable direct gas-phase ion generation at atmospheric pressure with minimal sample preparation, making them ideal for rapid and high-throughput analyses [19]. ESI, in particular, is widely used in both laboratory and POC diagnostics due to its ability to gently ionize large, thermally labile biomolecules with minimal fragmentation [20, 21].

The process begins with the application of a high voltage to a conductive liquid flowing through a narrow capillary. This generates a strong electric field at the capillary tip, typically around 10^6 V/m [21]. When the electrostatic forces exceed the liquid's surface tension, the meniscus deforms into a conical structure known as the Taylor cone, first described by Sir Geoffrey Taylor in 1964 [22]. At the cone's apex—where the electric field is strongest—charged microdroplets are emitted, forming a fine aerosol that initiates ion formation [20].

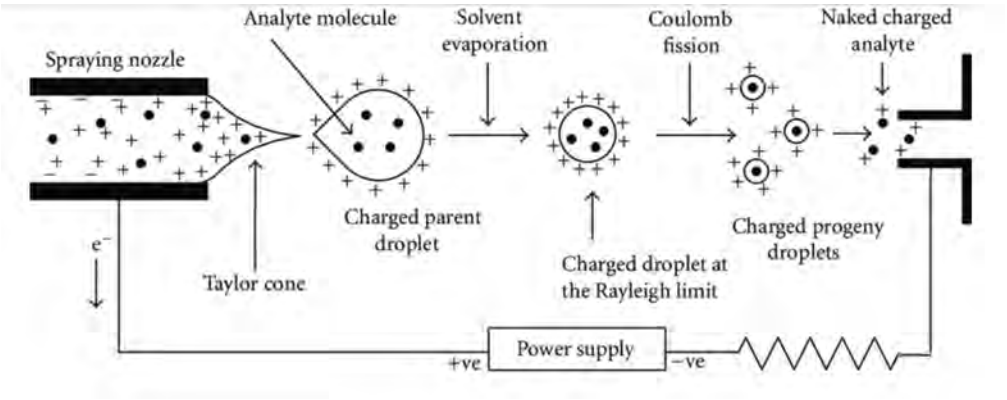

Figure 2.2 Schematic representation of the electrospray ionization process [6]reproduced under the terms of the CC BY 3.0 license.

As charged droplets travel toward the mass spectrometer, solvent evaporation gradually increases their surface charge density. When this density reaches the Rayleigh limit—where electrostatic repulsion exceeds the cohesive force of surface tension—the droplets become unstable and undergo Coulombic fission, breaking into smaller, highly charged progeny droplets [23]. This sequence of evaporation and fission repeats, progressively concentrating the analyte into nanoscale droplets, referred to as charged progeny droplets in Figure 2.2.

In the final stage, gas-phase ions emerge from these desolvated nanoscale droplets, shown as "naked charged analytes" in Figure 2.2. Two main mechanisms have been proposed for this transition. According to the charge residue model (CRM), continuous solvent evaporation leads to the formation of a single analyte molecule carrying the residual charge. Alternatively, the charge ejection model (CEM) suggests that analyte ions are directly emitted from the droplet surface once the electric field becomes sufficiently strong. Both mechanisms result in the production of free ions, which are subsequently transmitted into the mass spectrometer for detection and analysis [24].

It is worth noting that ESI can operate in either positive or negative mode, depending on the polarity of the applied voltage and the chemical nature of the analyte. In positive mode, analyte molecules (denoted as N) are typically protonated in the liquid phase, forming ions of the type $[N + H]^+$ via the reaction $N + H^+ \longrightarrow [N + H]^+$. This mode is particularly effective for compounds that readily accept protons, such as alkaloids, small peptides, and proteins. As a result, positive-mode ESI is widely applied in proteomics, metabolomics, and pharmaceutical analysis.

Building on ESI, several ambient ionization techniques have emerged, including LC-MS, Desorption Electrospray Ionization (DESI), and Direct Analysis in Real Time (DART), all

enabling direct analysis of complex samples with minimal preparation [10]. Among these, a notable development is Paper Spray Ionization (PSI), introduced by Liu *et al.* in 2010 [13], which has since attracted growing attention. Inspired by ESI, PSI replaces the traditional capillary with a porous paper substrate that transports the sample via capillary action. The wetted paper serves as a conductive medium, allowing ion generation under high voltage without the need for external pumps. This innovation gave rise to the PS-MS technique.

In the following section, we detail the underlying mechanism of ion formation in PS-MS.

2.2 PS-MS: principle and mechanism

Prior to discussing the mechanism of the PS-MS technique, it is important to first review the properties of the paper substrate.

2.2.1 Paper properties

Paper, a hydrophilic and porous material primarily composed of cellulose, has long been used in analytical techniques such as paper chromatography and colorimetric assays [25]. Its low cost, ease of modification, and ability to support capillary-driven flow make it an ideal substrate for diagnostics, including pregnancy tests and glucose monitoring [25].

Building on this foundation, Microfluidic Paper-based Analytical Devices (μPADs) have emerged as versatile platforms for chemical and biochemical assays, following the pioneering work of G. Whitesides et al. in 2007 [26]. These devices are created by patterning paper with hydrophobic barriers to form hydrophilic channels that autonomously transport small fluid volumes without external pumps [27]. By integrating fluid handling and detection onto a single patterned surface, μPADs function as paper-based lab-on-a-chip systems. This approach echoes the broader lab-on-a-chip concept, which seeks to miniaturize entire analytical workflows onto compact, self-contained platforms [28]. Because they are easy to use, inexpensive, and work well without complex equipment, paper-based lab-on-a-chip devices are ideal for testing outside of laboratories, including in clinics, remote areas, and on-site fieldwork [29]

Understanding fluid transport in porous media is essential for the design, use, and optimization of μPADs. Numerous computational models have been developed to simulate fluid imbibition at the microscale. However, these models often struggle to accurately capture fluid behavior at the larger scales characteristic of paper substrates [7].

2.2.2 Capillary flow modeling in paper-based devices

To address capillary-driven flow in porous structures, researchers have long relied on simplified analytical models. Among these, the most commonly used is the Lucas–Washburn model, originally formulated by Lucas (1918) and Washburn (1921). This classical model conceptualizes the porous medium as an assembly of idealized cylindrical capillaries and relies on a set of simplifying assumptions [7]:

- The pores are straight, cylindrical capillaries of uniform radius.
- The capillary walls are smooth and rigid.
- The contact angle between the fluid and the solid surface remains constant over time.
- The liquid exhibits Newtonian behavior and flows in a laminar regime.
- The system is fed by an infinite liquid reservoir.
- The region behind the advancing liquid front is fully saturated.

Within this framework, capillary forces promote fluid infiltration, while viscous drag acts as the opposing force. The resulting Lucas–Washburn equation describes the position L of the wetting front as a function of time t:

$$L(t) = \sqrt{\frac{\gamma\, r\, \cos\theta\, t}{2\mu}} \tag{2.1}$$

where, γ represents the liquid–air surface tension, r is the capillary radius, θ the contact angle, and μ the dynamic viscosity of the fluid.

For clarity, the Lucas–Washburn coefficient k is defined to characterize the rate of liquid front propagation in the capillary:

$$k = \frac{\gamma\, r\, \cos\theta}{2\,\mu} \tag{2.2}$$

While the Lucas–Washburn model provides useful insight into capillary-driven flow, it does not fully reflect the complex behavior of fluids in real porous materials such as paper. Unlike ideal capillaries, paper is composed of a random network of interwoven cellulose fibers that form a highly irregular and tortuous system of interconnected pores. In this structure, fluid flow is not governed solely by pore diameter; instead, it tends to follow the most continuous

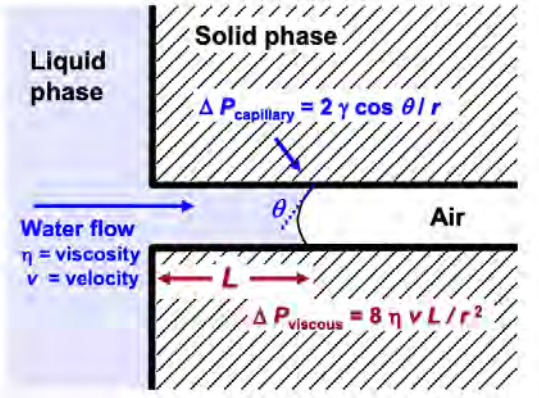

Figure 2.3 Illustration of capillary entry and the forces involved during liquid infiltration into a capillary [7]. Figure adapted from [7], licensed under ACS AuthorChoice for non-commercial use.

and accessible network of channels, regardless of their size. Experimental studies have shown that temporary blockages, irregular pore shapes, and fiber swelling can slow or divert the fluid, leading to uneven and unpredictable wetting fronts across the paper substrate [30].

To better represent flow at larger scales, particularly in fully saturated media, Darcy's law is often employed. This macroscopic model assumes an average pore geometry and a uniform saturation behind the liquid front. Darcy's law relates the volumetric flow rate Q through the porous medium to the pressure drop ΔP:

$$Q = \left(\frac{\kappa A}{\mu L}\right) \Delta P \tag{2.3}$$

In this expression, A is the cross-sectional area, L the flow path length, and κ the material permeability. The Lucas–Washburn law is a microscopic model describing liquid penetration in a single capillary over time, driven by capillary pressure and resisted by viscosity. In contrast, Darcy's law is a macroscopic model that relates the volumetric flow rate through a saturated porous medium to the pressure drop across it.

2.2.3 PS-MS mechanism

Leveraging the capillary properties of porous paper, PS-MS enables direct analyte ionization via spontaneous fluid transport. Combining the simplicity of disposable paper devices with the efficiency of PSI, it provides a rapid, low-cost, and user-friendly platform for chemical and biochemical analysis.

In general, the PS-MS process follows a sequence of steps described in the literature [13,14,31]. PS-MS uses a cellulose-based paper substrate, often cut into a triangle, onto which a small sample volume (typically 5–20 µL) is deposited near the base. This specific geometry provides an optimal configuration for PSI, offering stable spray formation—a feature discussed further in this review. The sample passively wicks through the porous matrix toward the tip. Simultaneously, a high DC voltage (typically between 3 and 5 kV) is applied to the rear of the paper, commonly via a metallic clip. Positioned near the grounded MS inlet, the tip accumulates charge, generating strong electrostatic forces. Although forming a well-defined Taylor cone in PSI is challenging due to the paper's geometry and material properties, a stable spray plume is still produced at the tip, governed by the same physical principles [9]. Ionization efficiency and spray stability in PSI depend on key experimental parameters such as paper geometry, solvent composition, and applied voltage [9].

In the context of PS-MS, the triangular paper substrate fulfills multiple roles simultaneously:

- It transports the solvent by capillary action toward the paper tip;
- It concentrates the electric field at the apex due to the geometric "tip effect";
- It facilitates the formation of the Taylor cone at the paper's extremity which plays the role of an emitter.

Figure 2.4 illustrates how PSI builds upon the principles of ESI by incorporating a porous paper substrate, thereby enabling the development of the PS-MS technique.

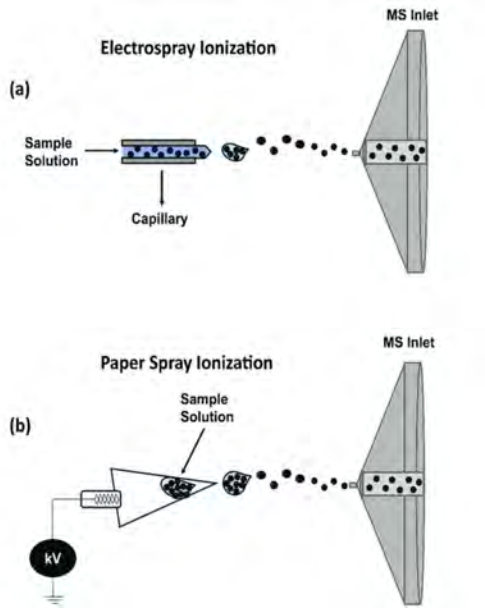

Figure 2.4 Schematic comparison between ESI and PSI. This illustration highlights the fundamental differences in device configuration, sample transport, and ionization principles between both techniques. Reproduced with permission from [8]. © Elsevier (License no. 6072140997821).

2.2.4 Spray plume characterization in PS-MS

The performance of PS-MS depends on several interrelated factors, notably the stability of the spray plume (*i.e.*, consistent formation of charged droplets over time), the efficiency of ion generation, and the reproducibility of the analytical signal. These parameters are all influenced by the physical characteristics of the spray. Nguyen *et al.* [9] showed that spray behavior in PSI is highly sensitive to variables such as electric field strength, solvent flow rate, paper thickness, pore size, tip angle, and surface chemistry. These conditions determine the formation of distinct electrostatic spray regimes, each of which influences the mechanism of droplet generation, droplet size and velocity, ionization efficiency, and temporal signal stability. As established by Espy *et al.* [8], the spray plume generated during PSI can be classified into three distinct modes based on the number and spatial distribution of liquid jets observed at the paper tip:

- **Single cone-jet** — Emission of a fine, charged jet from the center of the tip, forming a stable and focused spray. This regime offers optimal conditions for efficient and reproducible ionization.
- **Multi-jet mode** — Formation of two to three jets at distinct locations on the tip.

This regime is less stable than the single cone-jet and generally yields lower analytical reliability due to signal fluctuations.

- **Rim-jet mode** — Characterized by the emission of more than three jets distributed along the perimeter of the paper tip. While it can sustain high signal intensity, it introduces spatial inhomogeneity and compromises spectral resolution and reproducibility.

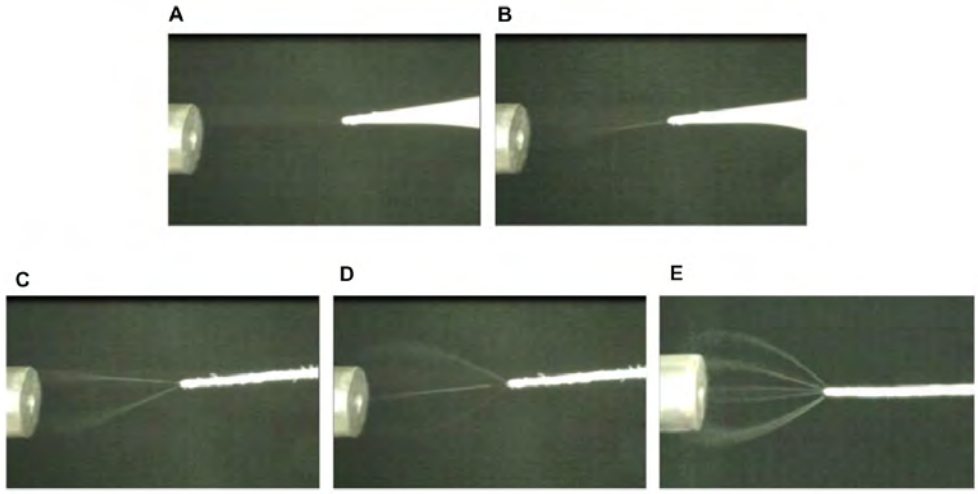

Figure 2.5 Images of spray plumes observed from the side of the paper substrate at increasing applied voltages, with a constant spray flow rate of 5 µL min^{-1}. (A) no visible spray jet; (B) single cone-jet mode; (C) multi-jet mode with two distinct jets; (D) multi-jet mode with three distinct jets; (E) rim-jet mode characterized by multiple jets distributed along the paper edge. Reproduced from [9], under the terms of the Creative Commons Attribution License (CC BY 4.0).

The applied electric field primarily controls the transition between spray regimes. As the voltage increases from 1.5 to 6.25 kV [8], the spray evolves from single-jet to multi-jet, and finally to rim-jet mode. Onset voltages are approximately 2.3 kV for the single-jet, 3.7 kV for the multi-jet, and 5.2 kV for the rim-jet mode [8]. At higher voltages, rim-jet dominates, emitting multiple jets radially along the paper tip due to electrostatic repulsion. This mode produces a higher ion current by generating more charged droplets. The enhancement stems from local electric field amplification caused by the fibrous paper structure, which—unlike smooth capillaries—offers numerous emission sites where individual fibers act as micro-emitters.

On the other hand, a mode like the single cone-jet one allows the formation of smaller droplets that present several advantages in the context of MS :

- They evaporate more rapidly,
- They promote more efficient ion release into the gas phase,

This leads to improved ionization efficiency. And ultimately enhances both the sensitivity and the signal intensity detected by the instrument.

Other spray modes can also be observed; however, they are generally undesirable. These unstable onset modes typically occur at low voltages or under non-ideal conditions, such as improper geometry or poor wetting. The dripping mode involves a slow, gravity-driven release of large droplets, leading to intermittent and inefficient signals. The pulsating mode is characterized by the periodic appearance and disappearance of the spray cone, resulting in fluctuating signal intensity and poor reproducibility.

In summary, each spray mode results in droplets with distinct properties, significantly impacting the ionization process and thus the overall efficiency of PS-MS, as reflected by the mass spectral signal [9].

2.3 Parameters influencing spray formation in PS-MS

2.3.1 Effect of the voltage on the efficiency of the spray

PS-MS is highly sensitive to variations in the local electric field at the emitter tip, which plays a critical role in the initiation and stability of the spray. The strength of the electric field E generated between the ESI emitter and the counter electrode (typically the inlet of the mass spectrometer) can be approximated by the following expression [9]:

$$E = \frac{V}{A \cdot r \cdot \ln\left(\frac{4d}{r}\right)} \tag{2.4}$$

where:

- V is the applied voltage,
- r is the radius of the emitter tip,
- d is the distance between the emitter and the counter electrode,
- A is an empirical constant that depends on the specific geometry of the system.

This relationship underscores the critical influence of the emitter tip radius and the emitter-to-detector distance on the electric field strength, which in turn governs the formation of the

spray plume and the overall efficiency of the ionization process. In brief, the electric field at the capillary emitter directly influences the spray modes.

On the other hand, the study [32] demonstrated that the emission radius r_e of the Taylor cone is determined by both physical and electrical parameters of the electrospray system :

$$r_e = \left(\frac{\rho}{4\pi^2 \gamma \tan\left(\frac{\pi}{2} - \vartheta\right)} \left[\left(\frac{U_a}{U_T} \right)^2 - 1 \right] \right)^{1/3} \left(\frac{\mathrm{d}V}{\mathrm{d}t} \right)^{2/3} \tag{2.5}$$

The following equation highlights the dependence of r_e on:

- the liquid density ρ,
- the surface tension γ,
- the cone angle,
- the applied voltage U_a and the threshold voltage U_T,
- the flow rate $\mathrm{d}V/\mathrm{d}t$.

This equation enables the characterization of the spray plume radius, thereby providing an estimate of the resulting droplet size.

In PS-MS, increasing the applied voltage enhances the electric field at the paper tip, allowing it to better overcome the solvent's surface tension. This leads to the formation of smaller droplets, which improve desolvation, thereby gas-phase ion formation and overall ionization efficiency. Conversely, higher surface tension or sharper cone angles can hinder droplet emission, reducing ionization performance.

However, voltages above 6 kV often result in corona discharge—localized ionization of air near the paper tip—which introduces electrical noise, generates reactive species, and disrupts spray stability [10, 33]. To ensure stable ionization and preserve analyte integrity, PS-MS is typically operated within a voltage range of 3–5 kV [10, 33].

2.3.2 Effect of off-axis distance and tip-to-inlet distance on spray behavior

Understanding droplet size evolution in the spray plume is key to characterizing ionization efficiency in PS-MS. Espy *et al.* [8] measured droplet size distributions along the spray axis and

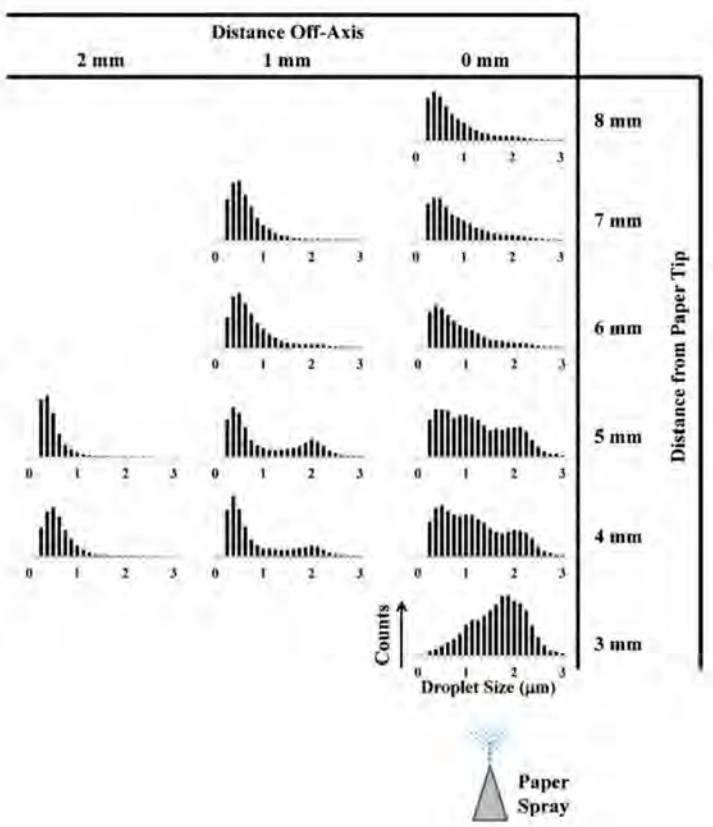

Figure 2.6 Droplet size histograms measured between 3 and 8 mm from the paper spray tip with a Phase Doppler Particle Anemometry (PDPA). The solvent was 80/20 MeOH:H_2O, with a flow rate of 5.0 µL min^{-1} and a spray voltage of +4500 V. Adapted from [8], under the terms of the Creative Commons Attribution License (CC BY 4.0).

at off-axis positions (Figure 2.6). Results show that droplet size decreases with distance from the paper tip due to solvent evaporation and Coulomb fission, while larger droplets dominate near the tip. Off-axis measurements revealed a high abundance of smaller droplets, likely emitted from peripheral jets. This spatial variation highlights the heterogeneous nature of PSI, influenced by localized electric fields and the paper's microstructure.

Together, axial and off-axis data provide insight into the physical mechanisms shaping droplet formation and evolution within the spray plume.

2.3.3 Effect of paper thickness

The thickness of the paper substrate is a critical geometric parameter in PS-MS, as it affects the sharpness of the emitter tip and the electric field distribution [9]. In single cone-jet mode, increasing thickness raises the onset voltage, which can be explained by treating the

thickness as the effective emitter radius in Equation 2.4. In contrast, rim-jet mode exhibits lower onset voltages with thicker paper, as the wider spacing between peripheral jets reduces electrostatic repulsion and promotes stable spray formation. For the multi-jet mode, onset voltage remains relatively unchanged, since the limited number of jets is already spaced far enough to minimize interaction.

Overall, paper thickness modulates both emitter geometry and jet distribution, depending on the spray regime. Optimizing this parameter is essential to achieving efficient and stable ionization.

2.3.4 Impact of solvent flow rate on spray mode and signal intensity

As shown by Nguyen *et al.* [9] and Vandergrift *et al.* [34], increasing the solvent flow rate from 20 to 80 μL/min at a constant spray voltage induces a transition in spray modes—from rim-jet, to multi-jet, and to the single cone-jet mode. This observation highlights that the spray mode is also influenced only by the quantity of solvent delivered to the paper tip. At lower flow rates, the solvent film is thinner, resulting in higher local charge density under the same electric field. This elevated charge density enhances electrostatic repulsion between the forming droplets, favoring the development of multiple rim-jets instead of a stable single cone-jet. Consequently, controlling the solvent flow rate is essential for achieving the desired spray mode. Nonetheless, lower flow rates produce smaller droplets, which evaporate more efficiently and thus improve ion desolvation and gas-phase ion production [8].

However, this introduces a trade-off: Lower flow rates produce smaller, highly charged droplets, enhancing ionization efficiency. Yet, very low flow rates tend to produce unstable spray modes (rim-jet or pulsating spray), which reduce reproducibility.

2.3.5 Effect of the properties of the paper surface on the spray mode

The wettability of the paper substrate plays a critical role in PS-MS ionization efficiency. Damon *et al.* [35] showed that optimal signal is achieved when the substrate's surface energy closely matches the solvent's surface tension. Highly hydrophobic papers impair wetting and destabilize Taylor cone formation, while overly hydrophilic ones absorb solvent too rapidly, limiting charge droplet accumulation at the tip and reducing ionization—especially at low voltages.

2.3.6 Role of the solvent in PS-MS

The physicochemical properties of the solvent—such as polarity, surface tension, volatility, and conductivity—directly influence the generation of charged droplets. When the solvent is poorly matched to the analyte or paper surface, or fails to support a stable Taylor cone, ionization efficiency may be significantly reduced, leading to suppressed signal intensity.

This phenomenon, known as ionization suppression, occurs when the ionization of a target analyte is reduced by co-existing compounds in the sample matrix. In PSI, analytes and matrix components compete for limited surface charge during droplet formation. More volatile, surface-active, or easily ionized species tend to dominate, reducing the signal of less competitive analytes. This can lead to significant signal loss, especially for low-concentration or poorly ionizing compounds. Optimizing the solvent is therefore essential to balance volatility, conductivity, and analyte affinity while minimizing matrix effects and enhancing PSI-MS sensitivity.

Furthermore, during the ionization, the evaporation of the droplets is not uniform: more volatile components (*e.g.*, water or organic solvents) are lost preferentially. As the solvent evaporates, the volume of the droplet decreases, but the amount of non-volatile solutes (including acids or buffer components) remains constant. This leads to an increase in solute concentration, which in turn lowers the pH of the droplet. This acidification effect has been well documented [36]. This pH shift can significantly alter the chemical environment within the droplet before complete desolvation and ion formation occur. For instance:

- It can change the protonation state of analytes, affecting their ionization efficiency.
- It may alter the charge state distribution, especially in sensitive species like proteins.
- It can even promote in-source chemical reactions, such as redox processes or fragmentation.

Selecting an optimal solvent composition in PS-MS remains a significant challenge [37]. Methanol/water mixtures are the most commonly used solvents, particularly in the analysis of proteins. As noted by Ueda *et al.* [38], conventional PS-MS workflows typically employ methanol–water systems for both small molecule and protein detection. Several reviews on ambient ionization techniques also highlight this solvent system as the standard in PS-MS for large biomolecules due to its ability to balance desolvation efficiency and ionization stability [14, 38]. Methanol, being highly volatile, facilitates rapid solvent evaporation and enhances droplet desorption, which is beneficial for ionization. However, solvents with

low surface tension, such as pure methanol, have a reduced capacity to sustain charge accumulation at the liquid–air interface. As reported by Girod et al. [39], this can result in poor charge density at the paper tip, impairing the formation of a stable Taylor cone. This highlights the need for careful tuning of solvent volatility, surface tension, and conductivity to ensure efficient and reproducible PSI operation.

2.3.7 Effect of the tip angle

As demonstrated by [10], tip sharpness plays a critical role in initiating the electrospray process in PSI. This requirement underpins the characteristic triangular geometry of paper substrates used in PSI. Electric field simulations have shown that the field intensity is maximized at the apex of the paper tip and increases as the tip angle decreases [10, 13, 40], as illustrated in Figure 2.7. In this context, the tip angle is widely recognized as a key geometric parameter influencing spray formation.

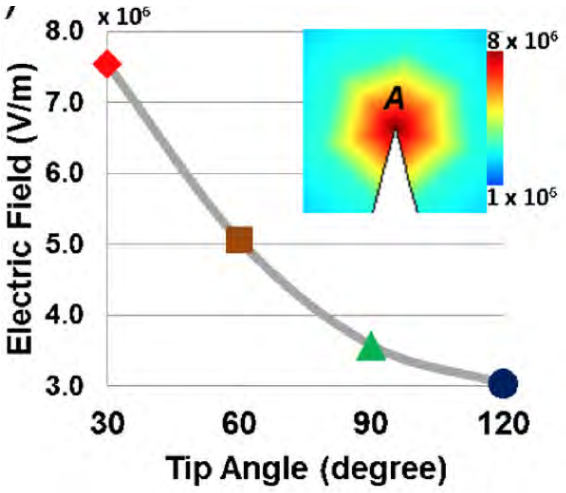

Figure 2.7 Electric field strength at the paper substrate tip as a function of tip angle for a given paper type and solvent system, as studied by [10]. Reproduced from [10], under the terms of the Creative Commons Attribution License (CC BY 4.0).

In general, tip angles between 30° and 45° are commonly reported to yield optimal ionization efficiency and signal intensity in PS-MS [40,41]. Angles sharper than 15° may lead to unstable sprays due to excessively narrow plume geometries, while very wide tips (*e.g.*, 150°) often fail to initiate any spray.

Zhu *et al.* [40] showed that reducing the tip angle leads to narrower spray plumes, enhancing the transmission of charged droplets into the mass spectrometer inlet. However, [10] highlighted that spray performance can vary with the type of paper, solvent system, and analyte,

suggesting that wider angles may still be effective in specific cases (see Figure 2.8).

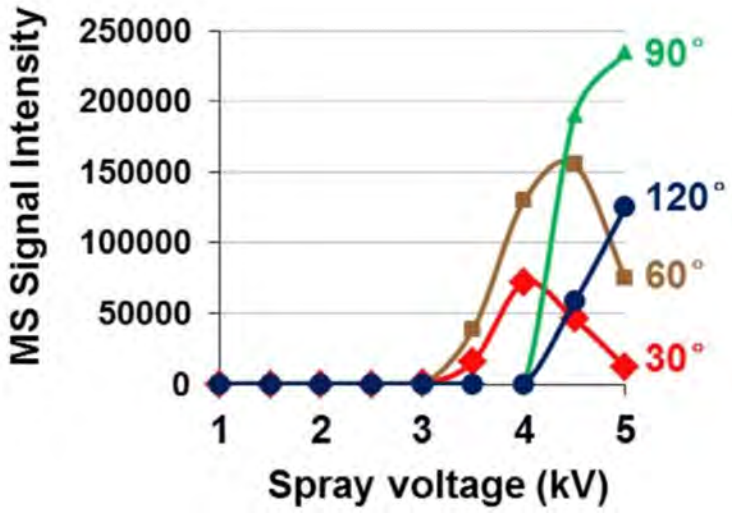

Figure 2.8 Relative mass spectrometric intensity for different tip angles (30°, 60°, 90°, and 120°) [10]. Note: this experiment depends on both the paper type and the analyte. Reproduced from [10] under the terms of the Creative Commons Attribution License (CC BY 4.0).

Despite these trends, a universal consensus on the optimal tip angle has not been reached. Several studies emphasize that spray performance is influenced by a complex interplay of variables, including the paper's physical characteristics (*e.g.*, thickness, porosity, and wettability), the solvent composition (surface tension, viscosity, volatility), applied voltage, ambient conditions, and the overall device design, including the distance between the paper tip and the MS inlet [41]. In summary, while sharper tip angles (typically below 45°) are generally advantageous for initiating and sustaining electrospray, their effectiveness is strongly modulated by other parameters. Optimal performance must therefore be assessed in the context of the complete system configuration, rather than relying on tip geometry alone.

2.4 Enhancements in PS-MS

2.4.1 Structural modifications of paper substrates

Conventional cellulose-based substrates can limit the sensitivity, reproducibility, or selectivity of PS-MS [10, 14]. To overcome these limitations, recent advancements have focused on substrate functionalization using materials like polystyrene microspheres, graphene, or carbon nanotubes [10,38]. These materials improve analyte extraction, ionization efficiency, and spray stability. Carbon nanotubes enhance ionization by increasing local electric field intensity [10]. Wang *et al.* reported that coating paper with polystyrene microspheres improved

sensitivity, with Limit of Quantification (LOQ) as low as 0.004–0.084 ng/mL [42]. Similarly, Ji *et al.* demonstrated that triangular devices coated with Mesoporous Graphene Foam (MGF) significantly improved analytical performance [43]. Their method achieved a 10-fold expansion in dynamic range, LOQ down to 1 pg/mL, and enabled detection in saliva using just 0.5 μL without pretreatment. Moreover, efficient ionization was achieved at reduced voltages (2.4 kV *vs* 3.5 kV). These functional coatings illustrate the potential of substrate engineering to enhance PS-MS sensitivity, selectivity, and robustness while preserving its simplicity.

2.4.2 Geometric advances in paper substrates for PS-MS

The geometry of the paper substrate plays a central role in the performance of PS-MS. Most commonly, a simple isosceles triangular shape is used, with the base serving as the sample loading zone and the apex as the spray tip. The dimensions and tip angle vary between studies, as they are often optimized based on the paper type, solvent system, and target analytes.

However, conventional geometries can be limited in controlling sample flow, spray reproducibility, or analyte retention. Recent studies have explored more sophisticated geometrical modifications to overcome these challenges.

One strategy involves embedding hydrophobic/hydrophilic microfluidic channels directly into the paper to better guide solvent flow and control droplet formation [44]. These guided pathways minimize analyte diffusion, improve reproducibility, and stabilize the spray. Additional innovations include the incorporation of sample reservoirs, defined storage zones, and multilayer paper designs, which help regulate solvent delivery and enhance desolvation [45]. Complex paper architectures—such as chevron patterns, branched channels, and 3D stacked layers—have been developed in PS-MS to enable sample pre-concentration, multi-analyte detection, and integrated fluidic control. These designs often incorporate additional components or materials into the paper structure to enhance functionality.

2.4.3 PS-MS development for clinical practices

PS-MS has shown strong potential for analyzing complex biological samples [46]. It enables direct testing of materials such as dried blood spots or urine with minimal sample preparation and can detect drugs at very low concentrations (ng/mL or lower) [37]. It has also been applied to distinguish lipid profiles in tissue samples, aiding in the differentiation between cancerous and healthy prostate tissue [47].

Although PS-MS is not yet widely adopted in clinical settings, multiple studies have demonstrated its ability to detect drugs at clinically relevant levels. For instance, Su *et al.* [37] successfully quantified eight drugs in whole blood, all at concentrations below typical therapeutic thresholds.

Protein detection using PS-MS remains more challenging due to strong adsorption of proteins onto paper fibers and reduced ionization efficiency with excessive solvent use [15, 31]. To address this, recent strategies—such as using synthetic paper [15], applying functional coatings like dendrimers or graphene foam [43], and incorporating printed microchannels and reservoirs [48, 49]—have significantly enhanced sensitivity, reaching detection limits below 1 pg/mL.

Despite these improvements, PS-MS is not yet a standard tool for clinical protein analysis. Further research is needed to optimize surface chemistry and develop robust workflows—such as on-paper enzymatic digestion—to support reliable protein detection in medical applications [46].

2.5 Challenges in PS-MS

Despite increasing interest in PS-MS for quantitative analysis, several key challenges hinder its reproducibility and broader adoption [13]. PS-MS performance is highly sensitive to variables such as paper type, tip geometry, solvent composition, and the distance between the paper tip and the mass spectrometer inlet. These factors directly affect ionization efficiency, spray stability, and detection limits. Another limitation is the risk of cross-contamination, which can arise either from chemical interactions with the paper substrate or from impurities inherent to the paper itself. To ensure analytical reliability, proper sample handling and thorough cleaning protocols are therefore essential [50].

PS-MS remains an incompletely understood technique. Ionization efficiency is influenced not only by the chemical properties of the analyte but also by the physical characteristics of the paper substrate—such as its porosity and possible tip deformation caused by gravity when the paper becomes saturated with solvent. These factors influence capillary-driven solvent transport and electric field distribution, both of which impact spray reproducibility. Sharper tip angles concentrate the electric field at the apex, enhancing ion emission [13], whereas excess solvent or drying can lead to an unstable signal.

In summary, while PS-MS offers great potential for fast, low-cost analysis of small molecules in biofluids, several issues must be addressed before the method can reach its full diagnostic potential:

- Standardization of paper substrates and solvent systems,
- Precise control of electrospray geometry and solvent flow,
- Improved compatibility with large biomolecules (*e.g.*, proteins),
- Integration into reproducible and portable diagnostic platforms.

CHAPTER 3 PROBLEM AND RESEARCH OBJECTIVES

3.1 Problem statement

While PS-MS has been relatively well characterized and successfully applied for the analysis of small molecules, important limitations remain—particularly regarding the comprehensive understanding of the underlying ionization mechanisms. No standardized protocol has yet been established, and PS-MS performance is highly sensitive to experimental conditions such as solvent composition, paper substrate type, and fabrication methods. Each of these factors can significantly influence signal intensity, ionization efficiency, and overall reproducibility. A deeper understanding of these dependencies is still needed to ensure consistent and reliable results across different laboratories and applications.

Moreover, the application of PS-MS to protein analysis remains limited. Proteins present additional challenges due to their high molecular weight, structural complexity, and broad charge state distributions under ambient conditions. These factors make them significantly more difficult to analyze than small molecules, and they currently hinder the broader adoption of PS-MS in proteomics and biomedical contexts.

In this study, we specifically focus on the characterization of PS-MS using a custom-designed μPAD developed in our laboratory, with the aim of analyzing proteins. As a model system, we selected myoglobin due to its well-known structure and relevance in biomedical research. Proteins such as myoglobin present greater analytical challenges than small molecules, owing to their higher molecular weight, complex tertiary structure, and less predictable ionization behavior under ambient conditions.

3.2 Objectives of the research

- To evaluate and characterize the performance of PS-MS technique under a range of experimental conditions using our custom-designed μPAD .
- To investigate the physicochemical properties and functional behavior of the paper substrates employed in the PS-MS configuration.
- To enhance our understanding of the fundamental mechanisms underlying PSI, including droplet formation, solvent evaporation (desolvation), and the generation of multiply charged ions.

CHAPTER 4 EXPERIMENTAL METHODS

4.1 Reactants and chemicals

4.1.1 Myoglobin properties

The protein selected as a model in this study to evaluate the PS-MS technique using our custom-designed device is myoglobin. Its key properties are summarized below [51]:

- **Number of amino acids:** 154.
- **Molecular weight:** Approximately 17,87 kDa.
- **Composition:** Hydrophobic core with a hydrophilic and charged exterior.
- **Isoelectric point (pI):** Between 6.8 and 7.3. At pH values below its pI, myoglobin carries a net positive charge due to a higher number of protonated groups.

Myoglobin exists in two forms: the **holo-form**, which includes the heme group (iron-containing cofactor), and the **apo-form**, which lacks this group. The presence of the heme stabilizes the protein's compact structure, resulting in lower charge states. Conversely, removal of the heme leads to partial unfolding and an increase in accessible protonation sites, yielding higher charge states in the mass spectrum [11].

Figure 4.1 3D structure of myoglobin containing the heme group. [11]

4.1.2 Solutions used in PS-MS Experiments

In order to investigate the effect of pH on the PS-MS experiments, acetic acid (CH_3COOH) was used as the pH-modifying component.

The solvent used for the PS-MS experiments consisted of a 1:1 (v/v) mixture of methanol and water, containing 50 µM myoglobin and a defined percentage x of acetic acid to adjust the pH. In total, three solutions with different pH values were prepared. The measured pH values are presented in Table 4.1.

Table 4.1 Measured pH of sample solutions composed of a 1:1 (v/v) mixture of methanol and water, containing 50 µM myoglobin and varying concentrations of acetic acid. The pH was determined by the Concordia laboratory using a pH meter.

Acetic acid concentration (% v/v)	**Measured pH and acidity description**
0.1%	Weakly acidic; pH = 3.3
1%	Moderately acidic; pH = 2.8
3%	Strongly acidic; pH = 2.0

All solutions were prepared by collaborators at Concordia University.

4.2 Material

In this study, four different types of paper used for the PS-MS experiments were purchased from Cytiva Whatman. These papers exhibit varying properties, notably in terms of thickness, porosity, and chemical composition. The characteristics of each paper type are summarized in Table 4.2. All of them are classified as filter papers.

Table 4.2 Characteristics of the different Whatman papers used in this study. All properties were obtained from the Cytiva Whatman manufacturor.

Paper Type	**Particle Retention (μm)**	**Thickness (μm)**	**Comment**
Whatman 1	11	180	
Whatman 2	8	190	
Whatman 4	20–25	205	
Whatman 114	25	190	High wet strength due to the addition of a small amount of chemically stable resin.

Note: Particle retention here refers to the material's capacity to retain particles of a given size, meaning it can effectively block particles equal to or larger than that size.

Note 2: Due to availability constraints, we used commercially available Whatman papers, where each pore size is associated with a specific thickness. As a result, it was not possible to independently control the pore size and thickness. This limitation is acknowledged and taken into account in the analysis.

4.3 Fabrication of the μPADs

This section focuses on the fabrication process of the device itself rather than on the design of its geometry. Indeed, the process used for the conception and development of the μPAD geometry was part of previous work and is described in Appendix B (Preliminary Work). The geometry was created using the FreeCAD software.

Triangular microfluidic devices were fabricated from Whatman filter paper and patterned using a Rayjet desktop laser engraver (Trotec). Laser cutting was performed using the following optimized parameters: power = 1,44 W, speed = 5mm/s, and frequency = 2000 Hz, to ensure precise geometry without burning or damaging the paper structure.

Each chip was laser-cut into an isosceles triangular shape with a height of 24.14 mm and a base width of 20 mm. The tip angle was adjusted according to the experimental conditions (15°, 30°, or 45°). The overall geometry of all μPADs, including the channel network and the

reservoir radius, remained identical; only the tip angle differed, with its dimensions specified individually for each design. A central microfluidic channel was integrated during the laser-cutting process, terminating in a circular reservoir shaped like a microbubble with a radius of 4.11 mm. This reservoir served as a liquid storage zone, allowing for controlled sample introduction into the porous substrate. The channel measured 8.43 mm in length and 2 mm in width. The geometrical details are presented in Figure 4.2.

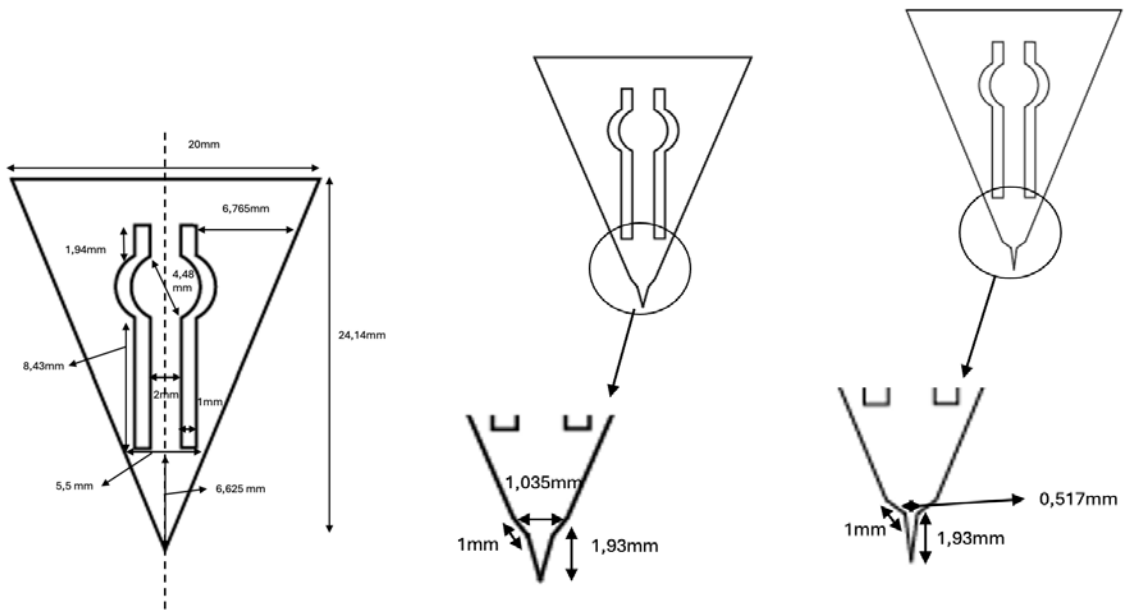

(a) μPAD with a 45° tip (b) μPAD with a 30° tip (c) μPAD with a 15° tip

Figure 4.2 Geometrical designs of the μPADs with three different tip configurations. Black lines indicate the laser cutting paths. All dimensions are given in millimeters (mm). Zoomed views of the triangular tips at 15° and 30° are provided to highlight the design differences.

After deposition onto the circular reservoir, the liquid flows toward the tip of the device by capillary action, guided by the linear geometry of the channel. A narrow region was preserved at the end of the channel near the spray tip to confine and direct the liquid flow (see Figure 4.2).

Following laser processing, the μPADs were cleaned using an ultrasonic bath to eliminate debris and potential contaminants induce in the paper and by the Rayjet desktop laser engraver (Trotec). Each chip was rinsed three times with ultrapure water (180 seconds per wash). This cleaning step is critical to avoid clogging at the tip, to preserve capillary-driven flow within the porous matrix, and to ensure reproducible and clean spray performance during analysis.

After cleaning, functional components were added. To ensure unidirectional flow of the liquid toward the tip a drop of epoxy resin was applied just behind the reservoir area and cured at room temperature for 48 hours.

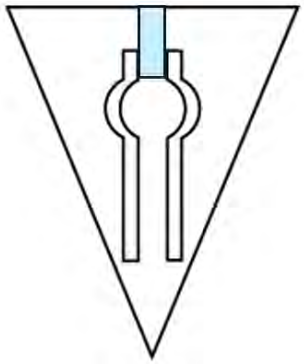

Figure 4.3 Schematic representation of the μPAD with epoxy coating highlighted in blue.

Finally, electrical contact between the solvent and the high-voltage power supply was established by attaching a strip of copper foil to the rear end of the paper device. This connection ensured a stable and efficient electrical interface during PSI.

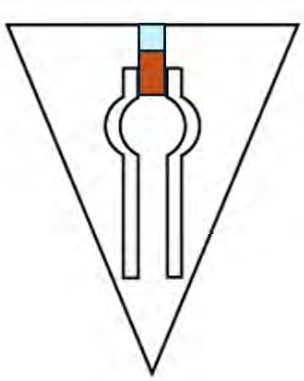

Figure 4.4 Schematic representation of the μPAD with epoxy (blue) and copper foil (orange-brown) additions.

Finally, the fabricated μPADs with different tip angles are shown in Figure 4.5.

Figure 4.5 Photographs of the three fabricated μPADs with different tip angles (15°, 30°, and 45°).

4.4 Electron Microscopy

Microstructural analysis was carried out using an Environmental Scanning Electron Microscope (ESEM) Quattro, available at Polytechnique Montréal in the Center for Characterization and Microscopy of Materials (CM)2. Quantitative measurements were extracted from high-resolution ESEM images using the ImageJ software, allowing for the estimation of geometrical pore sizes and structural features.

4.5 Flow rate analysis

To model liquid infiltration in the porous matrix, we used the classical Lucas–Washburn equation (Eq. 2.1). In the solvent wicking characterization, the objective was to track the position of the advancing liquid front over time. By fitting the experimental data to the Lucas–Washburn model, we estimated the solvent flow rate through the paper. For this purpose, rectangular strips of cellulose paper were laser-cut with precisely controlled dimensions (width 2 mm and length 12mm), incorporating a circular reservoir region at the base to mimic the geometry of the μPADs.

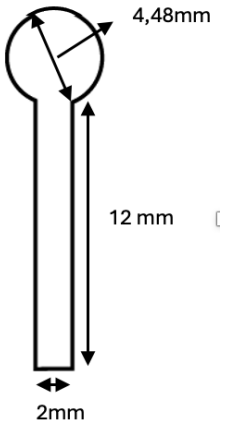

Figure 4.6 Schematic of the device used to determine the flow rate of the solvent for each type of paper.

A volume of 5 µL of a methanol:water mixture (1:1 v/v) was deposited onto the circular reservoir of each strip using a micropipette. The liquid infiltrated the paper via capillary action, forming a visible advancing front. As shown in Figure 4.7, the advancement of the liquid front within the paper strip is clearly visible over time. Figure 4.7a displays the liquid front at time t_1, while Figure 4.7b shows it at a later time t_2 ($t_1 < t_2$), illustrating the progression of the liquid front over time.

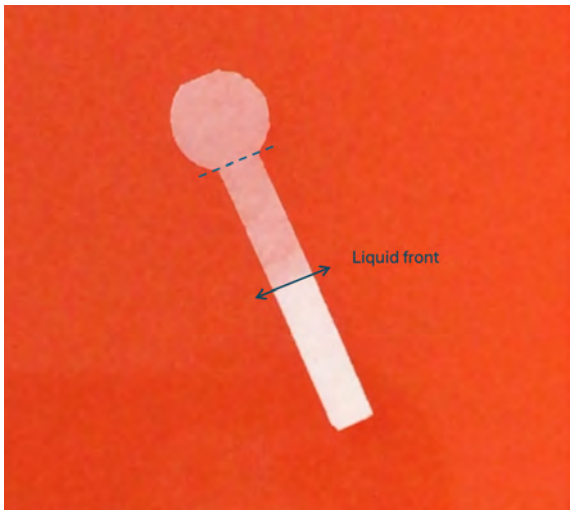

(a) Liquid front at t_1

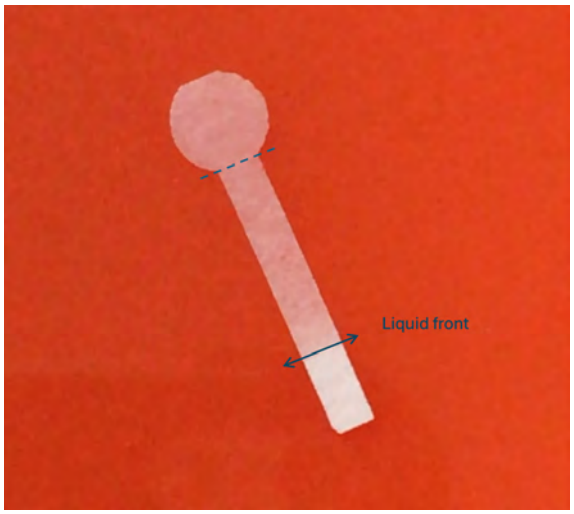

(b) Liquid front at t_2

Figure 4.7 Comparison of the liquid front positions at two different times ($t_1 < t_2$). The dotted line represents the initial position at time t=0, serving as the reference point for measuring the advancement of the liquid front.

The progression of this front was recorded using a smartphone camera. Subsequently, video analysis was performed using Movavi Video Editor 25 (temporal resolution of approximately 0.001 s), and the position of the liquid front at each time point was extracted using ImageJ, enabling high temporal and spatial accuracy.

The physical parameters of the methanol–water mixture used in the model are listed in Table 4.3, and are necessary for applying the Lucas–Washburn equation.

Table 4.3 Physicochemical properties of the methanol:water (1:1 v/v) mixture at 20°C.

Property	Value	Remarks / Source
Contact angle on cellulose	32–35°	Voda *et al.* [1]
Surface tension	40–42 mN/m	Interpolation between MeOH and H_2O
Dynamic viscosity	1.4–1.6 mPa·s	Voda *et al.* [1]

Note: Although resin was added to Whatman 114, its contact angle was not measured; for consistency and due to experimental constraints, the same value is assumed for all paper types.

4.6 Finite element modeling simulations

Finite element modeling (FEM) simulations of the paper-based chips were performed using COMSOL Multiphysics® version 6.1 (COMSOL Inc., Burlington, MA, USA).

4.7 PS-MS Experimental Setup

4.7.1 Mass Spectrometer Specifications

All experiments of PS-MS were performed using a high-resolution LTQ Orbitrap Velos mass spectrometer (Thermo Fisher Scientific) operating in positive ionization mode at Concordia Center for Biological Applications of Mass Spectrometry (CBAMS) located at Concordia University. See Table 4.4 for the technical specifications.

Table 4.4 Key specifications of the LTQ Orbitrap Velos mass spectrometer

Parameter	**Value**
Orbitrap resolution	Up to 60,000 at $m/z = 400$
Mass accuracy	< 2 ppm with internal recalibration
m/z range	Typically 50–6000
MS/MS acquisition rate	Up to 10 spectra/s
Ion trap	Dual linear ion trap (Velos)

4.7.2 PS-MS setup

Before doing PS-MS with our μPADs, as a control, solid triangular paper cut-outs (3 cm base $\times$ 2 cm height), without any microfluidic channel, were used. These served as negative controls to confirm that the spray effect was directly related to the presence of a functional microfluidic channel. For standard calibration, a 5 µM solution of crystal violet was used. Crystal violet was chosen due to its high ionization efficiency in positive mode and its characteristic purple color [52], which allowed for easy visual tracking of its migration through the paper substrate.

Prior to any electrical connection, the μPADs were mounted on the source platform and positioned approximately 5 mm from the inlet of the mass spectrometer. The copper foil located at the rear of the chip was then connected to the high-voltage probe. All high-voltage operations were conducted under safe and controlled conditions. A shielded and properly insulated high-voltage cable was used to connect the power supply to the probe. The high voltage remained off during installation to allow safe handling and secure clipping of the paper chip.

Only after the setup was fully completed was the high voltage applied. A voltage of 3.5 kV was used in positive ion mode to initiate the PSI process. Previous work conducted in the laboratory demonstrated that this voltage yields consistent and reliable results, making it well-suited for the optimized μPADs. Therefore, this value was used as the standard applied voltage for all subsequent PS-MS experiments.

Following μPADs positionning, the voltage turned off, and a small aliquot of 20 µL of the sample solution was deposited directly onto the reservoir of the chip to initiate ionization. The high voltage was then turned on.

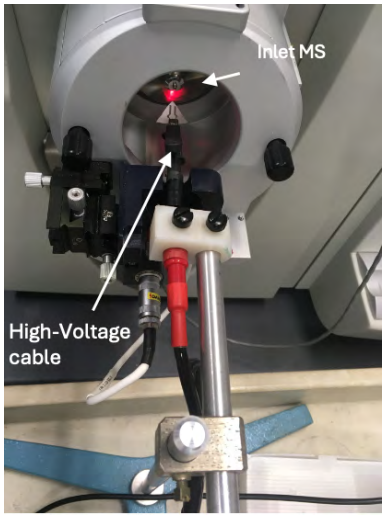

(a) View of the PS-MS experimental setup.

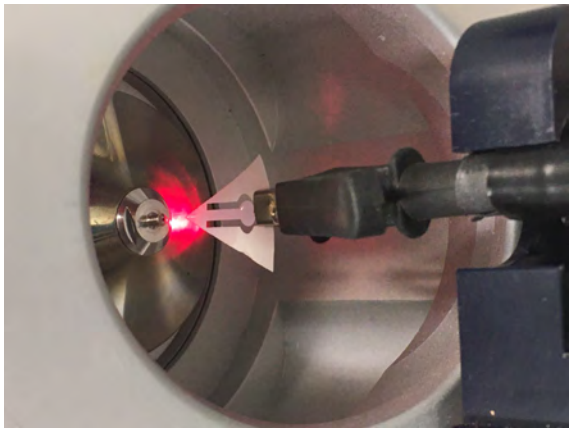

(b) Close up of the μPAD at the inlet of the mass spectrometer.

Figure 4.8 (a) and (b) illustrate the positioning of the μPAD and the overall mass spectrometry setup.

As soon as the high voltage was applied, mass spectra were continuously recorded over time. This allowed real-time monitoring of signal evolution, with the technician—responsible for both safety and instrument operation—observing the live intensity versus m/z traces using the Xcalibur software (Thermo Fisher), which enables the visualization and analysis of mass spectra. At this stage, the objective was to maximize signal intensity. For a particular device, during the acquisition, the chip's position relative to the MS inlet was adjusted to maximize the signal. The position was considered optimal once the spectrum stabilized and the signal reached a consistent maximum. The ionization process typically lasted for approximately between 1 and 2 minutes until the signal gradually diminished due to solvent evaporation (methanol being highly volatile).

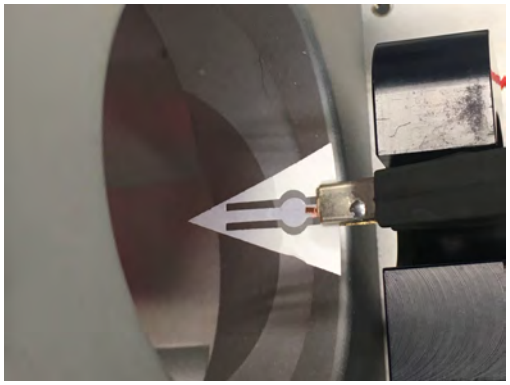

Figure 4.9 Photograph of the μPAD during PS-MS experiment.

Mass spectral data were acquired and processed using the Xcalibur software (see Figure 7.1).

4.8 Data analysis and statistics

Each mass spectrum obtained during the PS-MS experiments (see Chapter 7) was fitted with a Gaussian function to extract the peak center (μ), width (σ), and amplitude (A). This model provides a robust basis for comparing signal profiles, as mass spectral peaks typically exhibit symmetric, bell-shaped distributions due to instrumental and statistical effects.

In this context:

- A corresponds to the maximum intensity.
- μ represents the most probable charge state.
- σ reflects the spread of the charge state distribution.

Pearson's correlation coefficient (r) was calculated to assess the relationships between these Gaussian parameters and experimental variables, including tip angle, retention pore size, and a flow rate rank reflecting the paper's physicochemical properties. Correlations with $|r| > 0.5$ were considered significant.

CHAPTER 5 CHARACTERIZATION OF PAPERS

To characterize the microstructure of the paper substrates used in this study, ESEM technique was performed. The investigated materials included Whatman 1, Whatman 2, Whatman 4, and Whatman 114 filter papers as described in Section 4.2. ESEM provided valuable insights into fiber morphology, pore distribution, and surface roughness—key parameters that significantly influence capillary flow and spray formation in PS-MS.

5.1 Paper microstructure

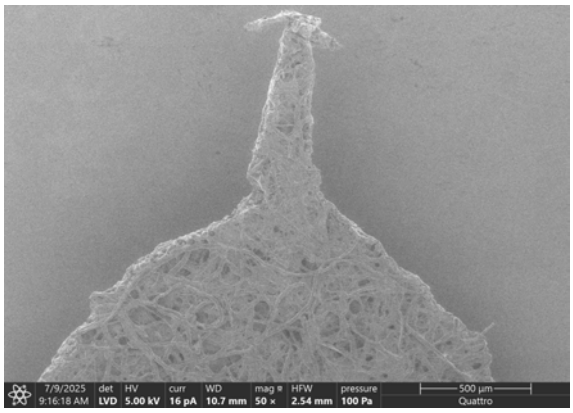

(a) Whatman 1 tip angle 15°.

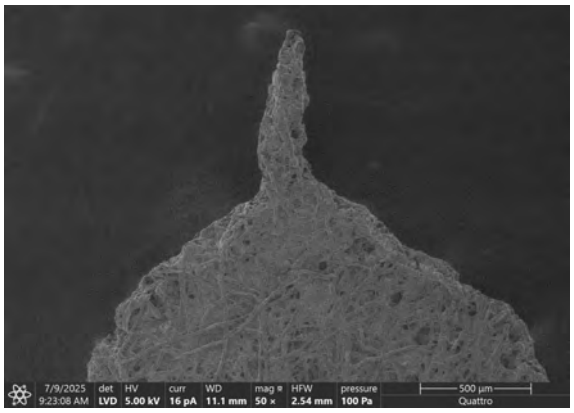

(b) Whatman 2 tip angle 15°.

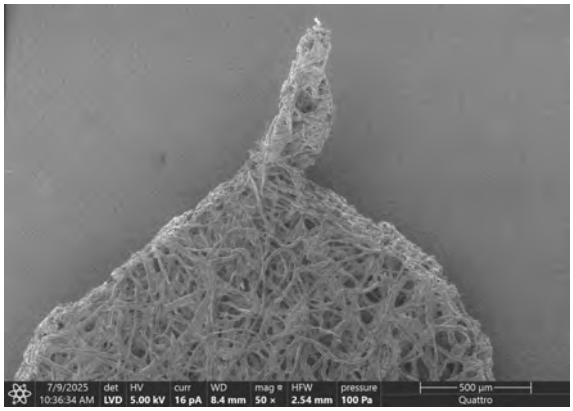

(c) Whatman 4 tip angle 15°.

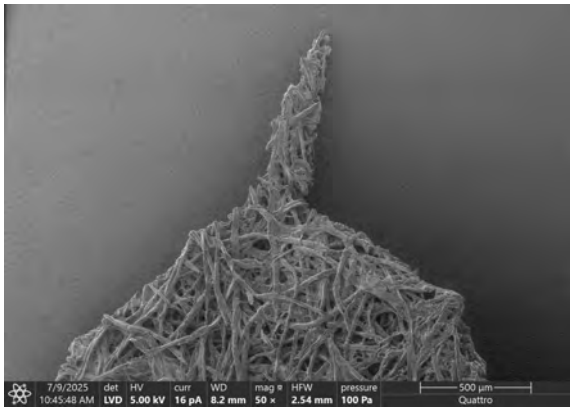

(d) Whatman 114 tip angle 15°.

Figure 5.1 ESEM images of the tip microstructure of Whatman 1, Whatman 2, Whatman 4, and Whatman 114 papers, all cut with a tip angle of 15° (magnification 50 ×).

Figure 5.1 shows that Whatman 2 exhibits a denser fiber network than the other Whatman paper types, while Whatman 1 presents a similar but slightly lower fiber density, consistent with the manufacturer's specifications. In contrast, Whatman 114 features a significantly more open structure, with no discernible resin layer observed at this magnification. A tip angle of 15° was arbitrarily chosen to illustrate the paper microstructure.

5.2 Tip angle characterization

This section is intended to illustrate the particular fiber arrangement at the tip right after the laser-cut process. As shown in Figures 5.2a and 5.2b, the fibers near the tip are oriented outward, acting as natural emitters that enable rim-jet or multi-jet mode formation. This effect varies with the tip angle but remains consistent across all paper types.

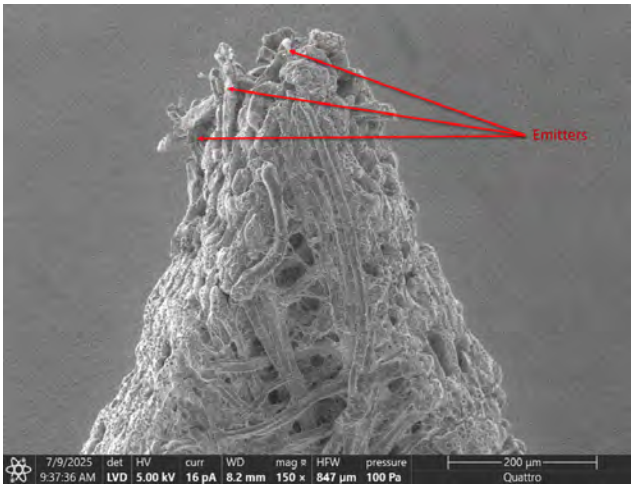

(a) Whatman 1 tip with a 45° angle at 150× magnification.

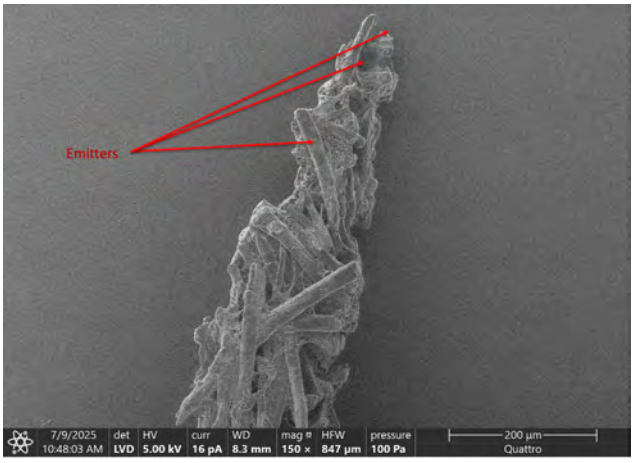

(b) Whatman 114 tip with a 15° angle at 150× magnification.

Figure 5.2 ESEM images of the microstructure near the tip region of laser-cut paper substrates. The red arrows indicate the natural emitters.

5.3 Flow rate analysis using the Lucas - Washburn model

This study investigated solvent flow rates in different paper types by measuring the advancement of the liquid front L over time. As shown in Section 4.5, the progression of the solvent front is clearly visible.

The measured liquid front positions $L(t)$ were fitted to the Lucas–Washburn equation (see Eq. 2.1) in order to extract the corresponding coefficients k (see Eq. 2.2), thereby characterizing the transport properties of the 1:1 (v/v) methanol–water mixture solvent used in

the PS-MS experiments (see Chapter 7). The validity of the model was confirmed by the linear relationship observed between L and $\sqrt{t}$ for all paper types. An illustrative example is provided in Figure 5.3, where the fitting curve demonstrates the expected linear dependence of distance on the square root of time.

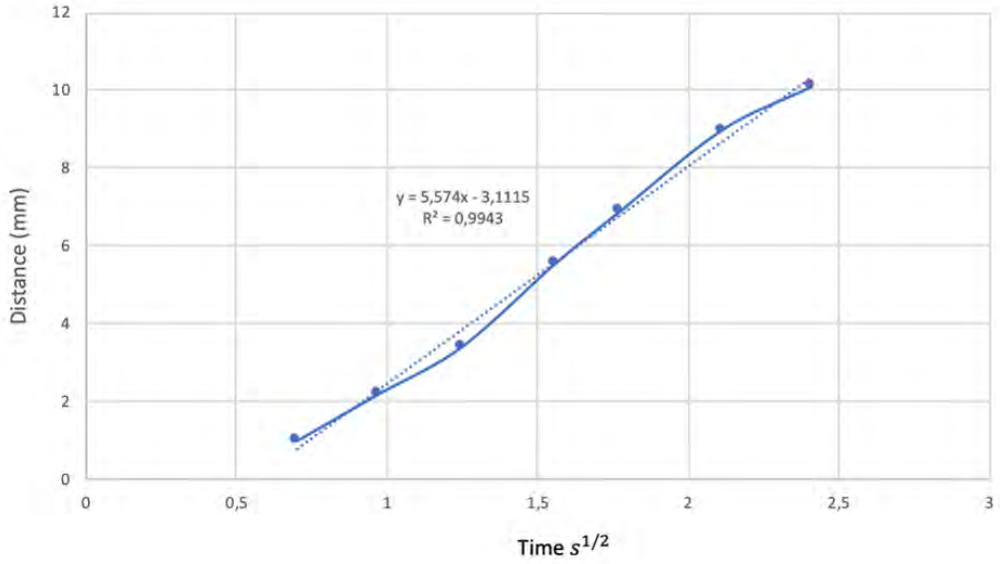

Figure 5.3 Liquid front progression over time using the Lucas–Washburn Model on Whatman 114 paper.

From the experimentally determined k values, obtained from three replicates per paper type, we estimated key parameters such as the pore radius r. The results, summarized in Table 5.1, are presented as mean ± SD (Standard Deviation) and compared with expected characteristics reported for each paper type.

Table 5.1 Lucas–Washburn coefficient and pore radius for different Whatman paper types. Values are given as mean ± SD.

Paper Type	Lucas–Washburn Coefficient ($cm \cdot s^{-1/2}$)	Pore Radius (µm)
Whatman 1	0.98 ± 0.13	8.53 ± 2.16
Whatman 2	0.84 ± 0.21	6.45 ± 2.91
Whatman 4	0.95 ± 0.041	7.82 ± 0.68
Whatman 114	1.10 ± 0.14	10.1 ± 2.55

Among the tested papers, Whatman 114 demonstrates the highest solvent flow rate, followed in decreasing order by Whatman 1, Whatman 4, and Whatman 2. The measured values are generally consistent with the commercial specifications (see Table 4.2). Indeed, Whatman 2

exhibits the lowest estimated pore size retention, which is in agreement with its Lucas–Washburn coefficient, remaining the lowest among the tested papers. In our experiments, Whatman 4 showed a slower wicking behavior than Whatman 1. One possible explanation lies in the thickness of the paper: although Whatman 4 has larger pores than Whatman 1, its greater thickness may allow more fluid to be absorbed overall, thereby affecting the observed front propagation rate. Additionally, Whatman 1 appears to behave slightly slower than Whatman 114, which is consistent with their structural properties. The presence of resin in Whatman 114 could increases its contact angle (although this was not measured, it can be hypothesized to be higher than in the other papers), thus influencing capillary flow dynamics.

These results confirm that the Lucas–Washburn model is applicable to our system. Additionally, they offer valuable insights into the relative capillary-driven solvent transport behavior for each paper type. Overall, this model effectively captures the influence of thickness, pore size, and composition in a single parameter.

5.4 Effect of epoxy on the paper microstructure

To further investigate the effect of epoxy application, we examined the microstructure of paper samples coated with epoxy. As shown in Figure 5.4, the epoxy effectively seals the pores of the paper. The resulting change in surface appearance and color reflects the presence of a uniform epoxy layer on the substrate. This color change can be attributed to the sealing of the pores and the formation of a continuous polymeric film. By reducing surface roughness and pore-induced light scattering, the epoxy modifies the optical response of the substrate. Furthermore, the difference in refractive index between cellulose fibers and epoxy alters light reflection and absorption, thereby contributing to the observed color change.

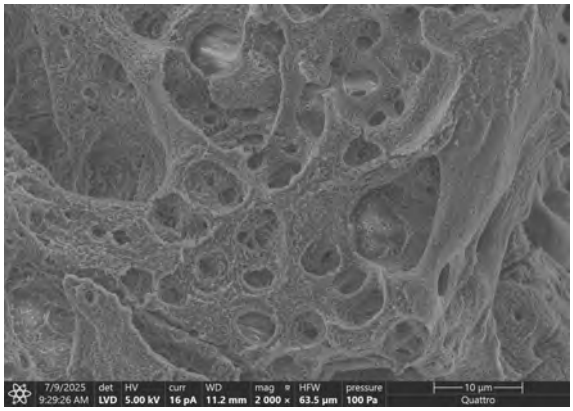

(a) Before epoxy

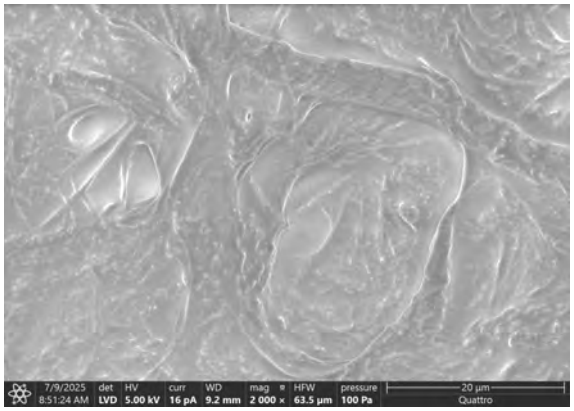

(b) After epoxy

Figure 5.4 ESEM images of the microstructure of Whatman 2 paper before and after epoxy application (magnification ×2000).

Figure 5.4 presents the case of Whatman 2; similar observations were made across all tested paper types.

5.5 Laser cut side effect

An ESEM image of the cross-section of the laser-cut paper reveals the presence of a thin deposited layer along the edges, suggesting that the tip region is not structurally homogeneous with the bulk of the paper. This localized modification is most likely the result of thermal effects induced by the laser cutting process. In this region, the overlap of two Gaussian beam profiles results in repeated exposure and intensified heating, effectively burning the edges twice (see explanation below). The exact nature and composition of this layer, however, remain to be determined and warrant further investigation.

This phenomenon is consistently observed in Whatman 1, 2, and 4, where a distinct edge layer appears following laser processing (see Figure 5.5a). In contrast, Whatman 114 exhibits a noticeably smoother and less rough edge surface (see Figure 5.5b). This difference may be attributed to the presence of a resin coating in Whatman 114, which could modify the material's interaction with the laser and affect the extent of thermal alteration.

(a) ESEM image of a Whatman 2 paper tip with a 30° tip angle, captured at ×2000 magnification.

(b) ESEM image of a Whatman 114 paper tip with a 45° tip angle captured at magnification x500

Figure 5.5 ESEM images of laser-cut paper tips showing microstructural features at the edge. A thin deposited layer can be observed in both cases, suggesting local thermal modifications due to the cutting process.

Moreover, during the fabrication of the μPADs tips by laser cutting, a discrepancy was observed between the angles defined in FreeCAD and the actual angles measured after cutting (see Figure 5.7). This mismatch is attributed to the finite focal width of the laser beam. Since the beam is conically focused, its waist defines a minimum cutting resolution: instead of producing a perfectly sharp intersection at the tip, the effective spot size broadens the cut and produces edges rounding (see Figure 5.6). The two edges of the laser that allow the cut of the chip tip partially overlap without converging to a mathematically sharp point. As a

result, the final geometry differs slightly from the intended design.

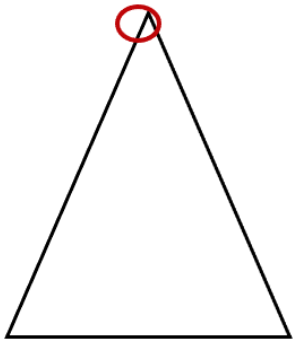

Figure 5.6 Schematic illustration of the laser beam focal path (red) intersecting the paper material (black lines) during cutting. Not drawn to scale.

To assess this effect, the tip angles were experimentally measured on Whatman 4 paper, used here as a reference substrate. In Figure 5.7, the nominal angles defined in the FreeCAD model are shown in black, while the values measured with ImageJ are highlighted in red. The measured angles were consistently larger than the intended ones, revealing a systematic deviation introduced by the laser cutting process. Although no statistical error analysis was performed (as only one measurement per design was taken), these results clearly demonstrate the inherent limitation of the method.

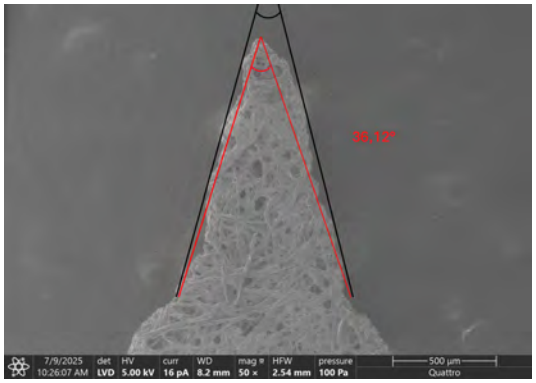

(a) Target angle: 15°

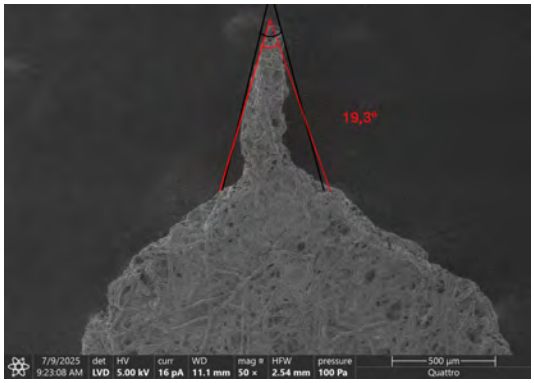

(b) Target angle: 30°

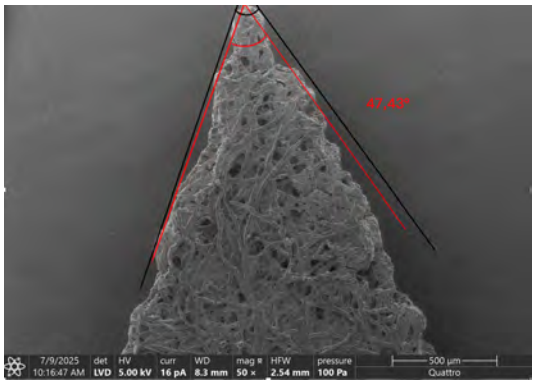

(c) Target angle: 45°

Figure 5.7 Tip angles obtained after laser cutting Whatman 4 paper. The nominal FreeCAD-defined angles are indicated in black, while the angles measured in ImageJ are shown in red.

For the remainder of this study, the experimentally measured tip angles are considered as the effective values. Although they differ from the theoretical ones, the order of magnitude remains consistent. To illustrate this deviation, consider the case of a tip defined with a nominal angle of 15°. This angle corresponds to a theoretical base width of:

$$b_{\text{theoretical}} = 2 \times h \times \tan(15^\circ) = 2 \times 2\,\text{mm} \times \tan(15^\circ) \approx 0.525\,\text{mm}$$

After cutting, however, the actual measured angle was 19.3°, corresponding to a base width of:

$$b_{\text{measured}} = 2 \times h \times \tan(19.3^\circ) \approx 0.7\,\text{mm}$$

The resulting difference in base width is:

$$\Delta b = b_{\text{measured}} - b_{\text{theoretical}} = 0.7\,\text{mm} - 0.525\,\text{mm} = 0.175\,\text{mm}$$

Assuming this excess width is symmetrically distributed on both sides of the tip, the effective laser beam radius at the focal point can be estimated as:

$$\boxed{r_{\text{focus}} = \frac{\Delta b}{2} = \frac{0.175}{2} = 0.0875\,\text{mm}}$$

These results suggest that the theoretical sharpness of a laser-cut tip is inherently limited by the focal spot size of the beam, which sets the minimum achievable resolution.

Although laser cutting cannot produce a perfectly sharp apex due to the finite beam waist and the Gaussian intensity profile, this limitation does not affect the functionality of the paper spray tip. The theoretical sharpness limit depends on optical parameters and varies with paper properties such as porosity and thickness. Calculating this limit precisely and optimizing for each material would require extensive calibration beyond the scope of this work. Instead, laser cutting provides sufficient sharpness, high reproducibility, and remains the most practical and scalable method for fabricating μPADs.

CHAPTER 6 COMSOL SPRAY SIMULATIONS

6.1 Model definition

A simulation was performed using COMSOL Multiphysics software to gain insight into the physical phenomena involved in PS-MS. The simulation domain consists of a porous medium surrounded by air, representing the typical paper–air interface encountered during PSI. The porous medium is modeled as a triangular domain, replicating the geometry of the experimental chip tip and obeying Darcy's law for fluid flow in porous materials. To model the PSI process, a static high voltage was applied between the base of the triangular chip (serving as the anode) and a fine rectangular electrode (representing the grounded mass spectrometer inlet), thereby reproducing the experimental conditions used to initiate spray.

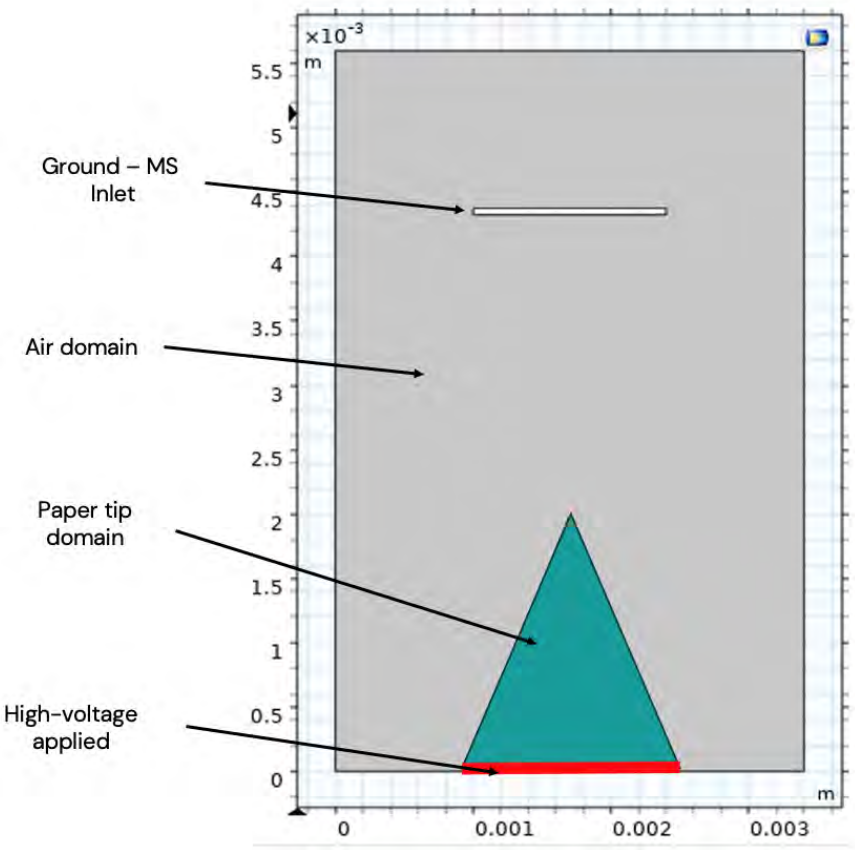

Figure 6.1 COMSOL Multiphysics interface used for simulating PSI at a 45° tip angle.

In this COMSOL simulation, the paper tip is considered pre-soaked with liquid and already saturated at time $t = 0$. At that moment, a high voltage of 3.5 kV is applied across the

system to simulate the experimental triggering of the electrospray process.

6.1.1 Physics interfaces

The following physics interfaces are used in the COMSOL model:

- **Laminar Flow** – includes the volume force from the electric field.
- **Level Set** – used to track the fluid–air interface.
- **Electrostatics** – defines the applied potential and resulting electric field.
- **Darcy's Law** – governs fluid transport within the porous paper substrate, accounting for permeability and porosity.
- **Multiphysics Couplings** – enables interactions between fluid flow, electric forces, and interface tracking.

6.1.2 Initial conditions

- **Laminar Flow:** The air domain was initialized with zero velocity and zero pressure to simplify the simulation ($\vec{u}_0 = 0$ m/s, $p_0 = 0$ Pa).
- **Electrostatics:** No initial electric potential or electric field distribution was defined within the domain.
- **Porous Medium:** The liquid was absorbed by a horizontally oriented paper sheet. Since gravity acts vertically while the paper lies in the horizontal plane, no vertical liquid column could form. Consequently, no hydrostatic pressure gradient developed along the paper, and the Darcy pressure was considered zero ($p_{\text{Darcy}} = 0$ Pa).

6.1.3 Boundary conditions

- **Laminar Flow:** A constant pressure outlet condition was applied ($p = 0$ Pa) at the exit of the geometry. This allows fluid to exit the domain freely while preserving a realistic interface between the fluid and air.
- **Level Set:** An open boundary condition was imposed to allow free evolution of the interface without artificial confinement.
- **Electrostatics:** A constant voltage condition was applied at the electrodes.

6.1.4 Geometric conditions

The air domain had a height of 5.6 mm and a width of 3.4 mm. The ground electrode was arbitrarily defined with a width of 1.4 mm and a height of 0.005 mm. To reflect realistic experimental conditions, only the paper tip was modeled as a triangular geometry with a fixed height of $y_{\text{tip}} = 1.982$ mm, while the base width varied depending on the tip angle:

- 15° tip angle: base width = 0.5175 mm
- 30° tip angle: base width = 1.035 mm
- 45° tip angle: base width = 1.525 mm

For all tip angles, the vertical distance between the paper tip apex and the center of the ground electrode was fixed at $h = 2.95$ mm. Although this value does not exactly match the experimental tip-to-inlet distance, it was chosen to simplify the simulation and ensure numerical stability. Both the tip apex and the center of the ground electrode were aligned along the x-axis at $x_{\text{tip}} = 1.7$ mm. .

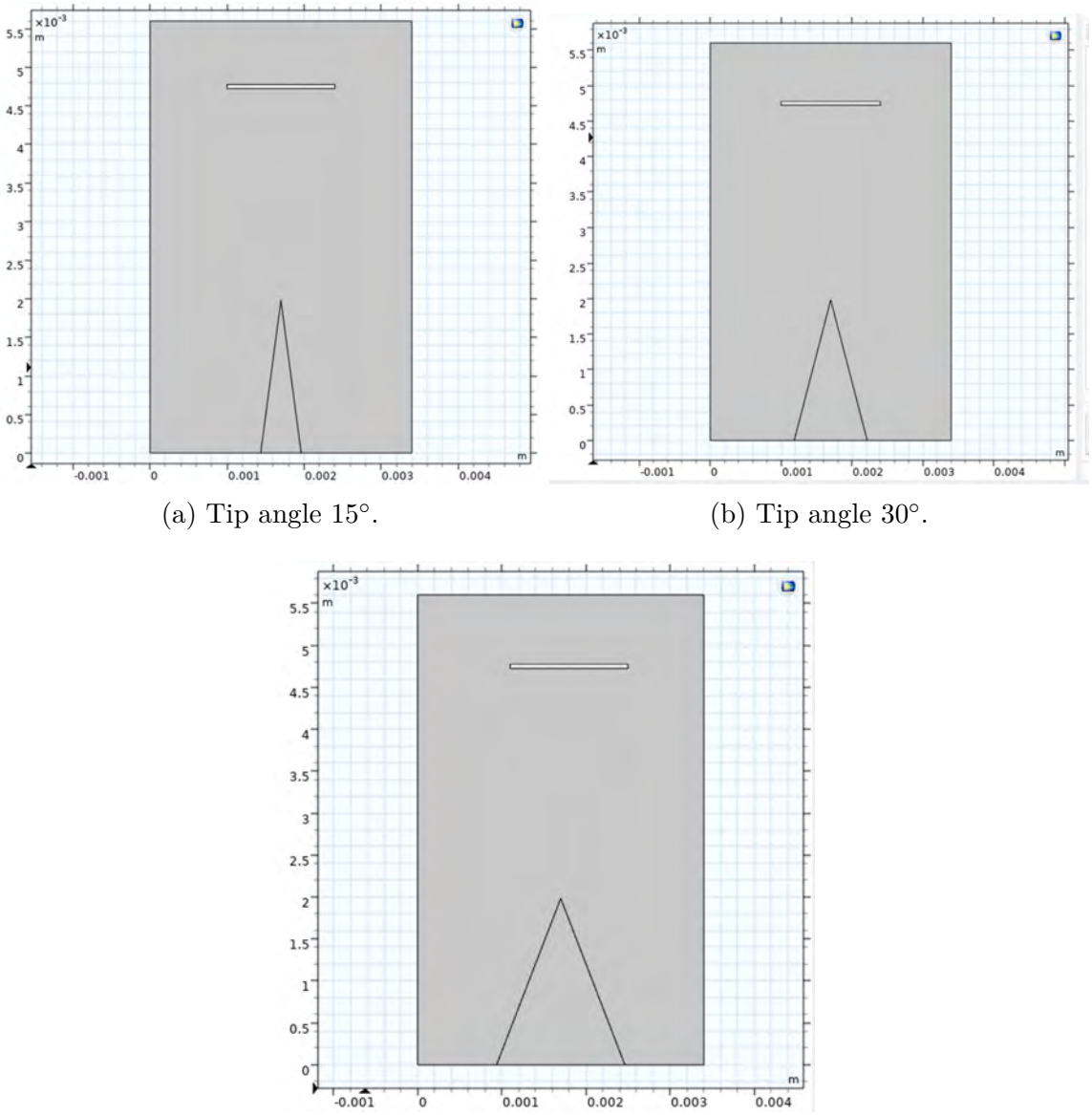

(a) Tip angle 15°.

(b) Tip angle 30°.

(c) Tip angle 45°.

Figure 6.2 COMSOL domain and geometry configurations for tip angles of 15°, 30°, and 45°.

6.1.5 Parameters considered

The simulation parameters were selected according to the solvent system used (1:1 v/v methanol–water) at different pH values (see Table A.1 in Appendix A). The paper properties correspond to Whatman 1 and are summarized in Table 6.1 below.

Table 6.1 Physical parameters of the paper used in the simulation, consistent with reported values for Whatman 1 filter paper.

Parameter	**Value (Symbol)**
Relative permittivity	$\varepsilon_r = 2.06$
Porosity	$\phi = 0.48$
Pore size retention	$r_p = 5.5 \times 10^{-6}$ m
Paper thickness	$t = 0.180$ mm

Note: The physical properties of Whatman 1 filter paper used in the simulation are based on manufacturer data (Cytiva Whatman manufacturer and [53]).

The parameters listed in Table 6.1 are kept constant for all simulations presented in the following sections.

6.2 PSI COMSOL Simulations

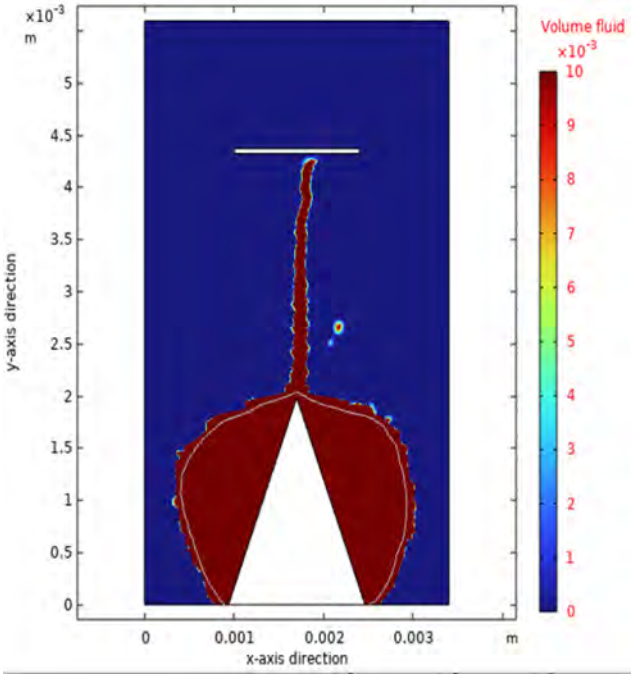

(a) Liquid volume visualization during PSI at time t = 0.126 s .

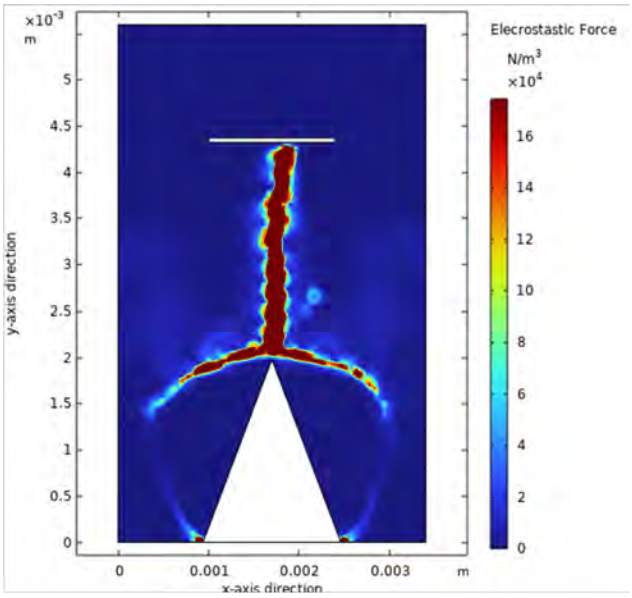

(b) Electrostatic force within the liquid during PSI at time t = 0.126 s.

Figure 6.3 PSI COMSOL simulations for the 45° with pH 3.3 at $t = 0.126s$

The simulations shown in the Figure 6.3 correspond to a tip angle of 45° as an example. The red region in Figure 6.3a shows the liquid moving toward the grounded electrode during the PSI process, while Figure 6.3b displays the corresponding electrostatic force acting within this liquid domain. More particularly, we display the electrostatic forces distribution at the apex of the tip at time t = 0.

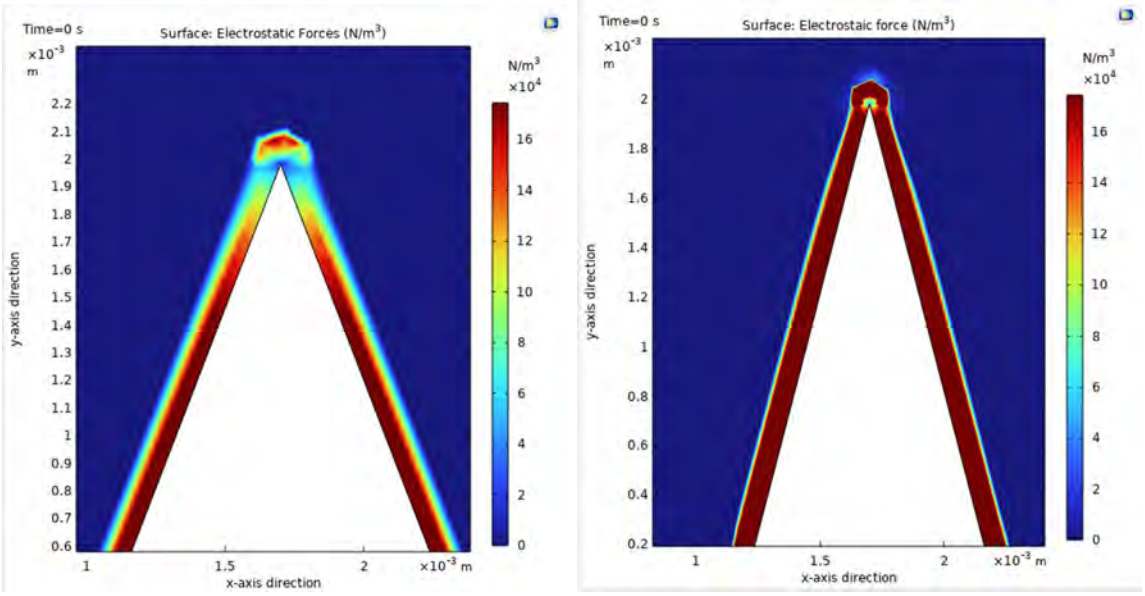

(a) Tip angle of 45° (b) Tip angle of 30°

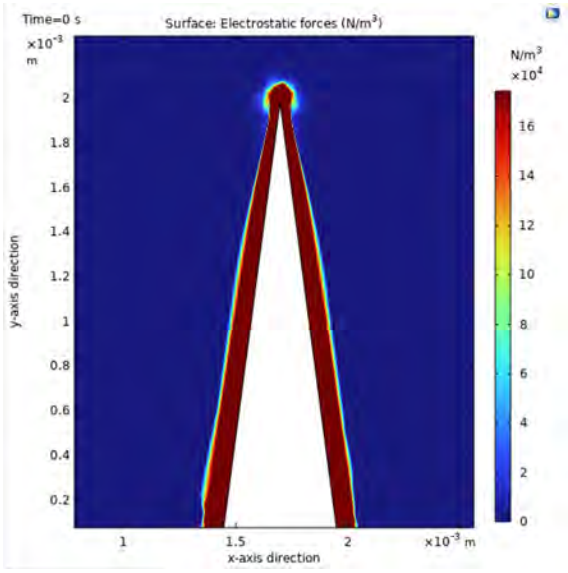

(c) Tip angle of 15°

Figure 6.4 COMSOL simulations of the electrostatic force distribution for three different tip angles: (a) 15°, (b) 30°, and (c) 45°, using a solvent with pH=3.3 at $t = 0$

In the following simulations, we focus on the electrostatic force distribution around the apex of the tip for different solvent pH values and tip angles for the same type of paper at time t = 0.

6.2.1 Electrostatic force distribution for the different tip angles

In order to characterize and compare the electrostatic forces across the different tip angles, we consider the following mapping domain:

- $x \in [x_{\text{tip}} - 0.4\,\text{mm},\ x_{\text{tip}} + 0.4\,\text{mm}]$,
- $y \in [0\,\text{mm},\ 2.2\,\text{mm}]$,
- with the tip coordinates defined as $(x_{\text{tip}}, y_{\text{tip}}) = (1.7,\ 1.982)\,\text{mm}$, corresponding to the position of the extreme point of the triangular tip.

The selected area was discretized into 100 horizontal slices along the y-axis. For each slice, only values exceeding 10^4 N/m^3 were considered. This threshold was arbitrarily chosen in order to eliminate background noise and residual artifacts.

The mean electrostatic force of the retained values was then calculated for each y-level. The corresponding results are presented in Figure 6.5 and summarized in Table 6.2.

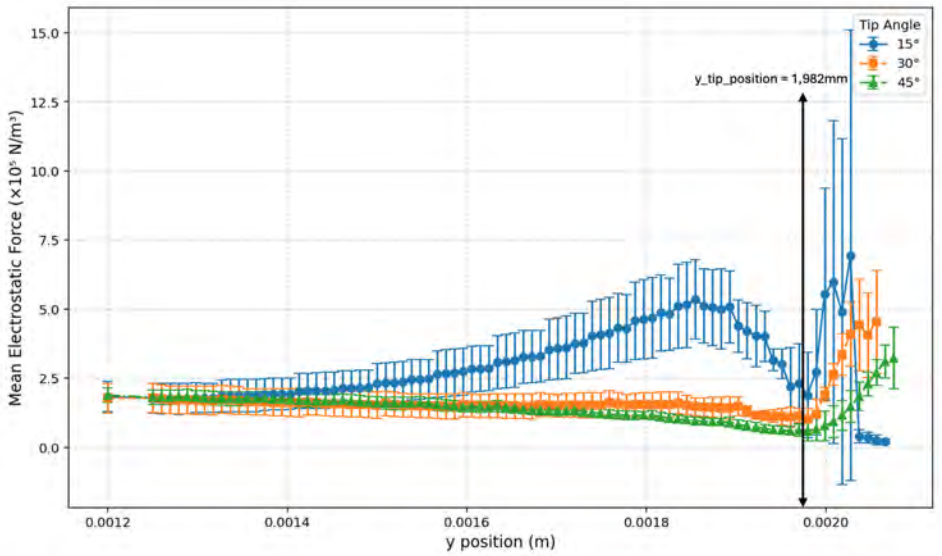

Figure 6.5 Comparison of mean electrostatic force profiles for different tip angles (15°, 30°, and 45°). Forces are averaged over y positions and include standard deviation as error bars. The simulation was made for Whatman 1 parameters and a solvent of pH=3.3. The tip position along the y-axis is given by $y_{\text{tip}} = 1.982$ mm.

Table 6.2 Summary of electrostatic force (mean ± SD) for different tip angles for a solvent at pH = 3.3.

Angle (°)	Force (N/m^3)
15	$(3.01 \pm 1.37) \times 10^5$
30	$(1.69 \pm 0.64) \times 10^5$
45	$(1.44 \pm 0.49) \times 10^5$

Figure 6.5 and Table 6.2 clearly show that a sharper tip angle (*e.g.*, 15°) leads to stronger electrostatic forces near the tip region, compared to wider angles for a pH=3.3. This trend is consistent across all tested pH values.

Moreover, as shown in Figure 6.6, for all tip angles, the simulation reveals a tip-enhanced electrostatic force distribution, forming a localized high-intensity lobe near the chip tip extremity. This region may play a critical role in the ionization efficiency of PS-MS.

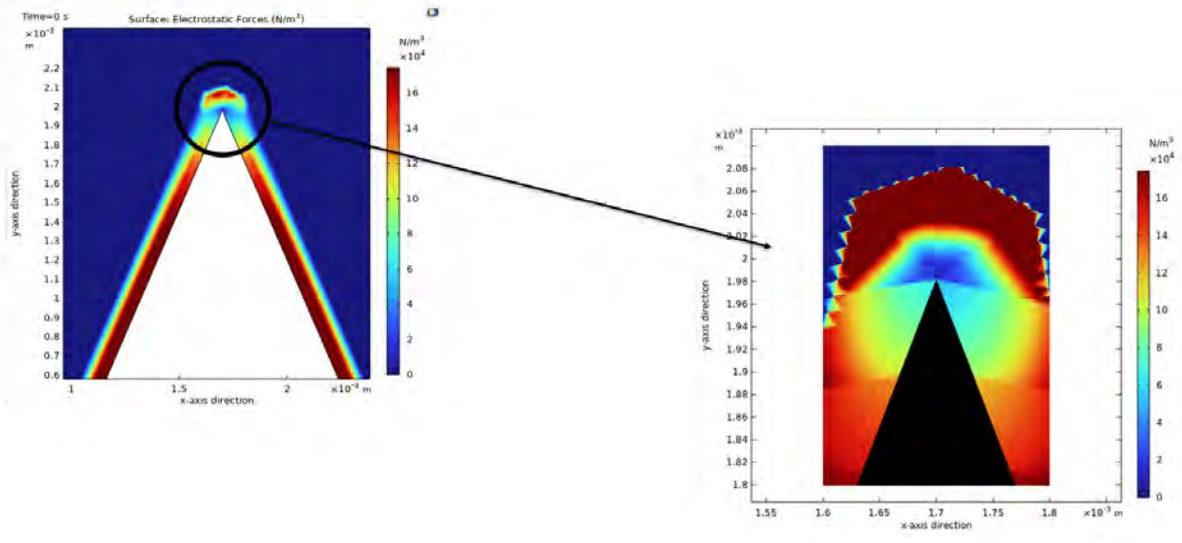

Figure 6.6 Zoom on the electrostatic region bubble for the 45° tip angle.

Electrostatic focusing at the tip apex for fixed angles and different pH values

The electrostatic force distribution was evaluated at each point $x \in [x_{\text{tip}} - 0.1 \text{ mm},\ x_{\text{tip}} + 0.1 \text{ mm}]$ along the line defined by $y_{\text{tip}} = 1.982$ mm. This analysis was carried out for all tip angles under different solvent pH conditions. Figure 6.7 shows the electrostatic force maps from which the values were extracted.

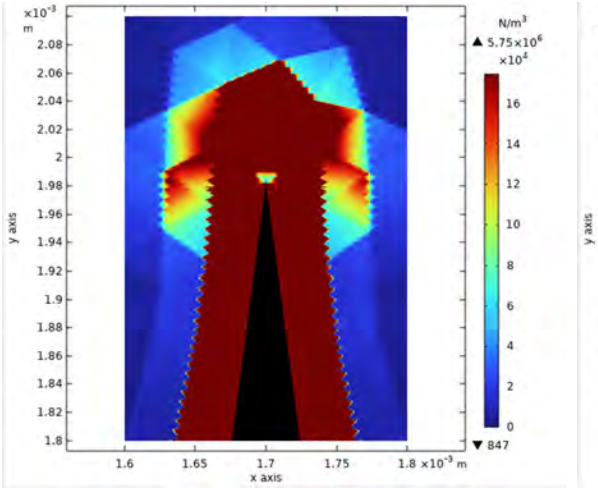

(a) Tip angle of 15°.

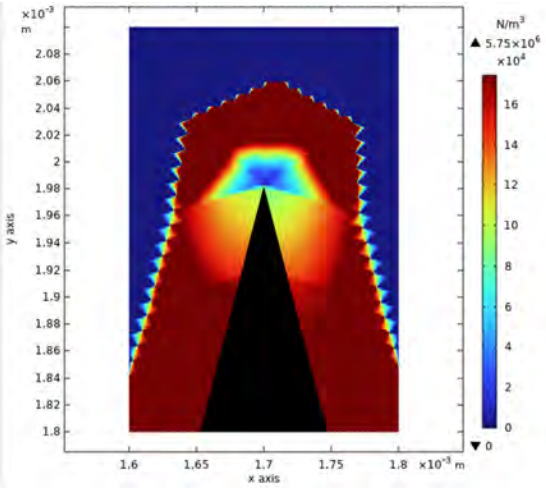

(b) Tip angle of 30°.

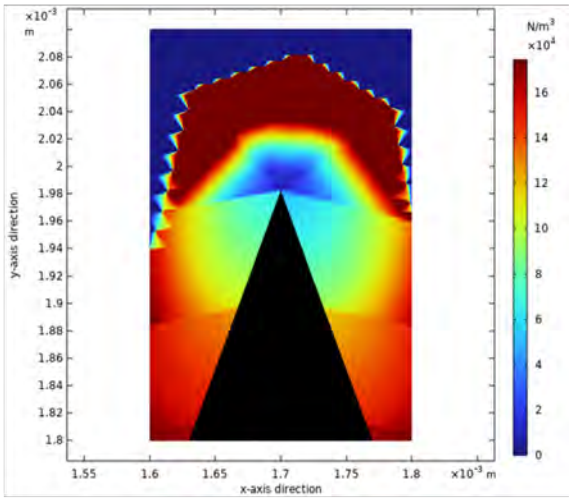

(c) Tip angle of 45°.°

Figure 6.7 Color maps of the electrostatic force distribution simulated in COMSOL for three different tip angles (15°, 30°, and 45°) under identical conditions using a pH 3.3 solvent.

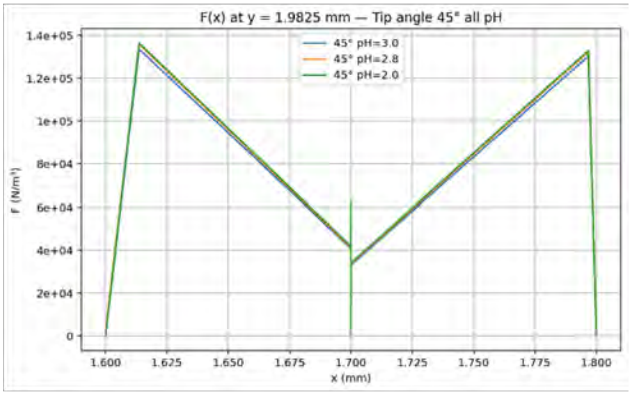

(a) Tip angle of 45°.

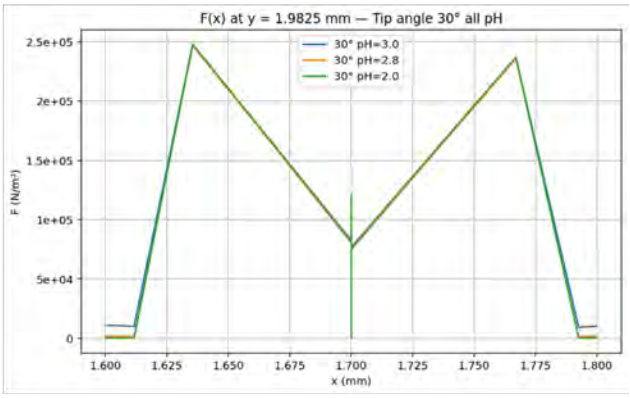

(b) Tip angle of 30°.

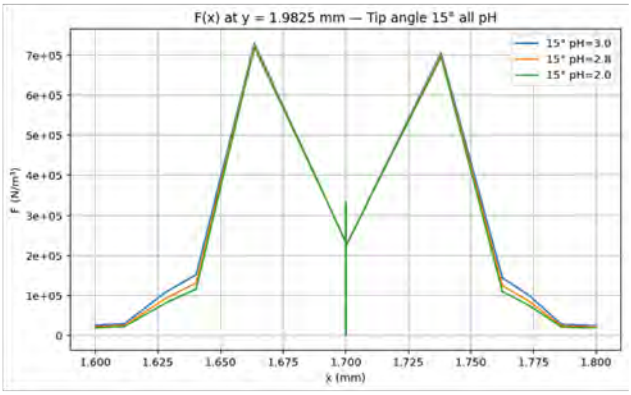

(c) Tip angle of 15°.

Figure 6.8 Comparison of electrostatic force profiles along the x-axis at $y_{\text{tip}} = 1.982\,\text{mm}$ for different tip angles (15°, 30°, and 45°) at different pH values (3.3, 2.8, and 2.0).

From Figure 6.8, it can be observed that the electrostatic force distribution is more focused and concentrated for the tip angle of 15°.

Electrostatic focusing near the tip at fixed pH and different tip angles

The electrostatic force distribution at a fixed pH was then examined for the different tip angles.

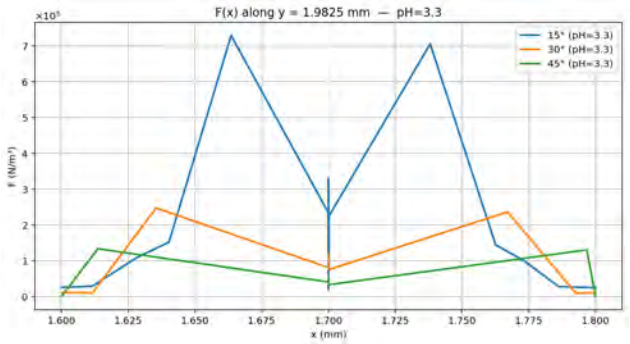

(a) pH = 3.3

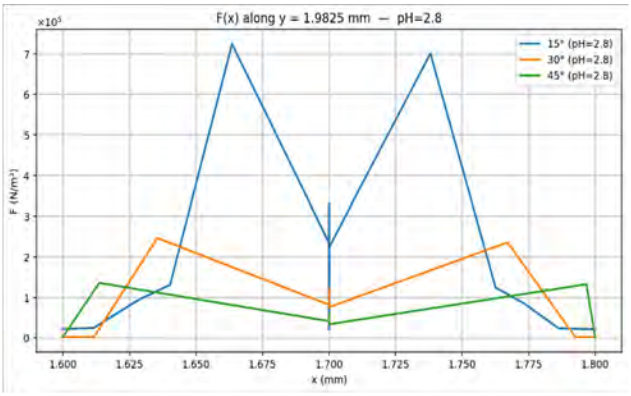

(b) pH = 2.8

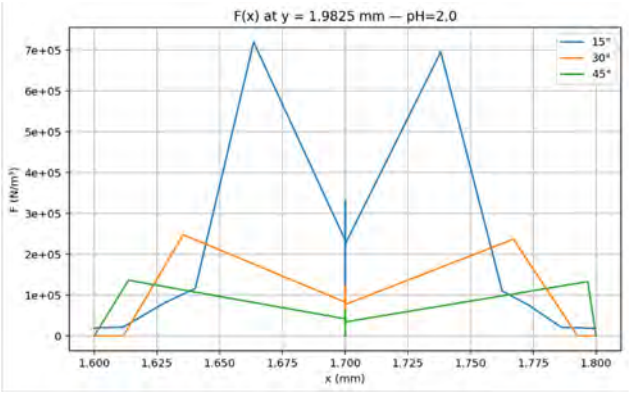

(c) pH = 2.0

Figure 6.9 Comparison of electrostatic force profiles along the x-axis at $y_{\text{tip}} = 1.982\,\text{mm}$ for different pH values (3.3, 2.8, and 2.0) at different tip angles (15°, 30°, and 45°).

Figure 6.9 illustrates the influence of tip geometry on the electrostatic force distribution under identical pH conditions. At constant solvent pH, the 15° tip produces stronger electrostatic confinement near the apex compared to larger angles. This effect can be attributed to a shorter conduction path for the 15° tip, while the cross-sectional area remains constant due to identical paper thickness. Consequently, the electrical resistance is lower for smaller tip angles. In contrast, larger tip angles spread the electric field over a wider area, reducing field intensity and increasing resistive behavior. All the Whatman papers have shown the same tendency. Furthermore, the same tendency has been observed when we change the distance from the tip to the MS inlet along the axial direction.

Although the simulated angles do not perfectly reflect the fabricated tip shapes, they provide meaningful insight into the role of apex geometry in PSI. The deviations observed in real samples likely have a limited effect on the qualitative conclusions drawn from the simulations. Future studies could further investigate the effect of tip rounding through extended simulations.

CHAPTER 7 PAPER SPRAY MASS SPECTROMETRY EXPERIMENTATIONS

In this section, a series of PS-MS measurements were conducted to evaluate the influence of paper geometry and its intrinsic properties—particularly their physicochemical interactions with the solvent—and the solvent pH on the signal obtained for myoglobin detection. Special emphasis was placed on the impact of these parameters on droplet formation, desolvation, and the charge state distribution during the generation of multiply charged ions.

Accordingly, several key parameters affecting PSI performance were investigated:

- **Tip Angle:** Tip angles of 15°, 30°, and 45° were investigated.
- **Paper Type:** The effects of pore size and thickness were evaluated using four commercial paper substrates : Whatman 1, Whatman 2, Whatman 4, and Whatman 114 (see Table 4.2). Two key indicators were considered: the Lucas–Washburn solvent flow rate coefficient, used to establish a flow rate ranking, and the pore size retention capacity.
- **pH:** To assess the influence of proton availability on ionization efficiency, three solvent pH values were investigated: 2.0, 2.8, and 3.3.

The solutions used for pH adjustment in the paper spray experiments are described in Section 4.1.2. The geometries of the paper substrates are detailed in Section 4.3, and correspond to the specific Whatman papers listed in Table 4.2. Overall, multiple parameter combinations were tested, such as Whatman 1 at pH 2.0, Whatman 1 at pH 2.8, Whatman 1 at pH 3.3, Whatman 2 at pH 2.0,.. Overall, 36 combinations were tested. Throughout all subsequent experiments, a constant voltage of 3.5 kV was applied (see Appendix B).

Pearson correlation analyses were performed between the parameters describing the myoglobin mass spectral response (amplitude A, center μ, and width σ) and the properties of the paper substrates (tip angle, pore size retention, and flow rate ranking), as well as the solvent pH. Further details on the statistical analysis are provided in Section 4.8.

7.1 Results and Discussion

7.1.1 Detection of myoglobin

In all PS-MS experiments, various protonated myoglobin ions—each associated with a specific mass-to-charge ratio (m/z)—were successfully detected by the mass spectrometer. Fig-

ure 7.1 presents all charged species observed during the spray period for a specific parameter combination including solvent-related components and potential chemical byproducts. Their chemical identities were confirmed by comparison with reference values reported in the literature, as myoglobin is a well-established standard in mass spectrometry studies, a procedure performed by my colleague Adam Bouguila at Concordia University. Mass spectrometry data were acquired by Jingsuy Sun and Dr. Hang, also members of Concordia University.

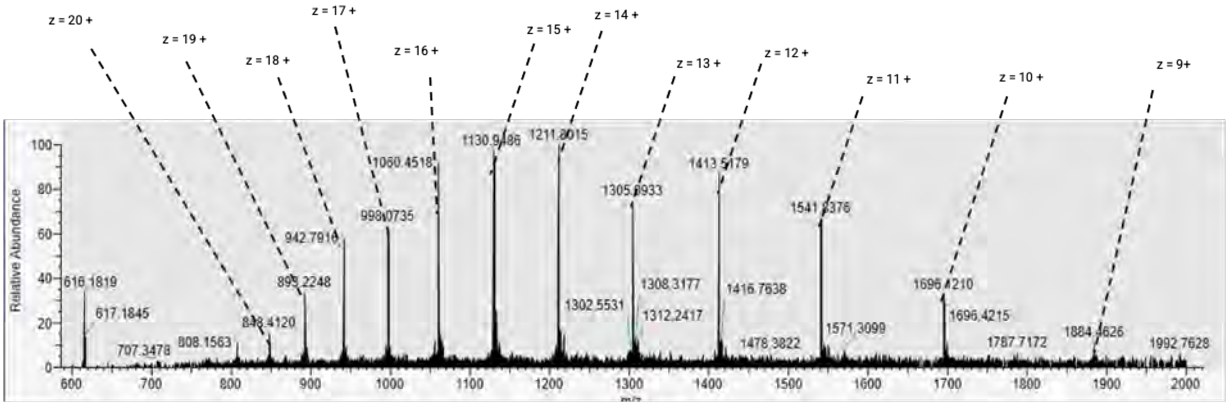

Figure 7.1 Mass spectrum of protonated ions obtained from the PS-MS experiment using the pH = 3.3 solvent at a tip angle of 45° using Whatman 1 paper with our custom-designed μPAD using the Xcalibur software. Charge state z related to the peaks and so to the ions detected are noted.

To facilitate spectral analysis and improve interpretability, all spectra—conventionally plotted versus m/z—were re-expressed in terms of the charge state z using the known molecular mass of myoglobin (see Section 4.1.1). For each spectrum, the corresponding Gaussian fit was overlaid on the same graph. As an illustration, the result corresponding to Figure 7.1 is shown in Figure 7.2.

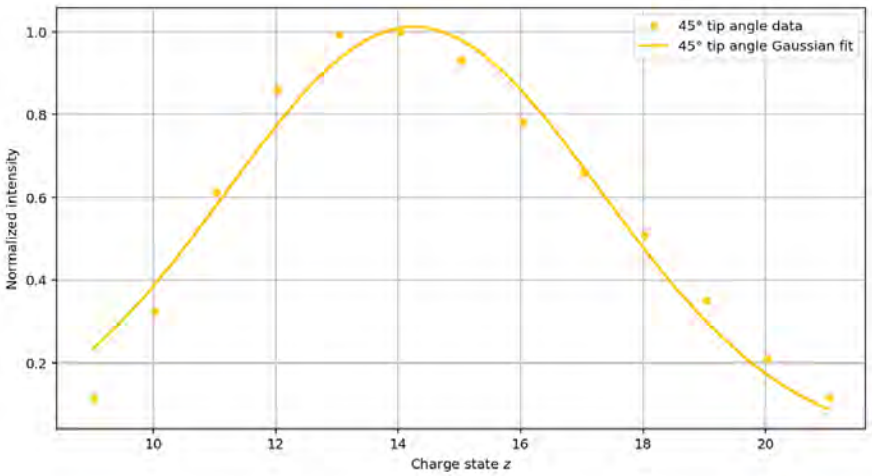

Figure 7.2 Relative abundance of protonated ions obtained from the PS-MS experiment using pH = 3.3 solvent, a tip angle of 45° and Whatman 1 paper with our custom designed μPAD.

To assess the stability of the spray over time, the normalized standard deviation of the relative abundance was calculated throughout the spray duration. As illustrative examples, Figures 7.3 to 7.5 present spray duration profiles observed across several PS-MS trials.

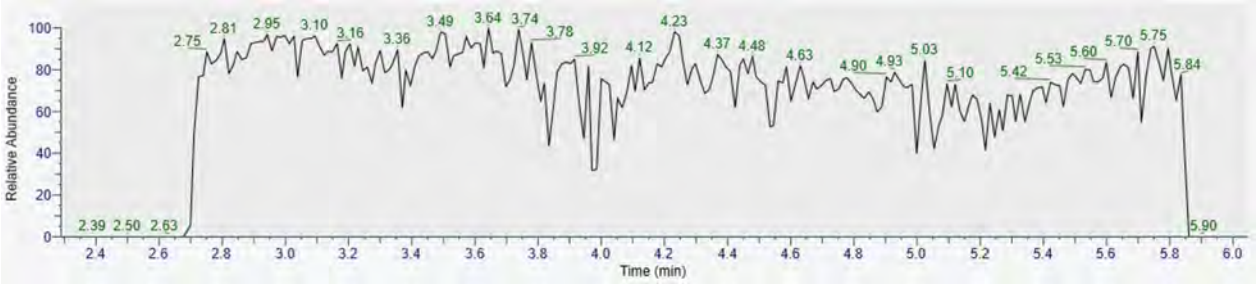

Figure 7.3 Example of spray duration observed using Whatman 2 paper with our custom designed μPAD at a tip angle of 30° and a pH of 2.8.

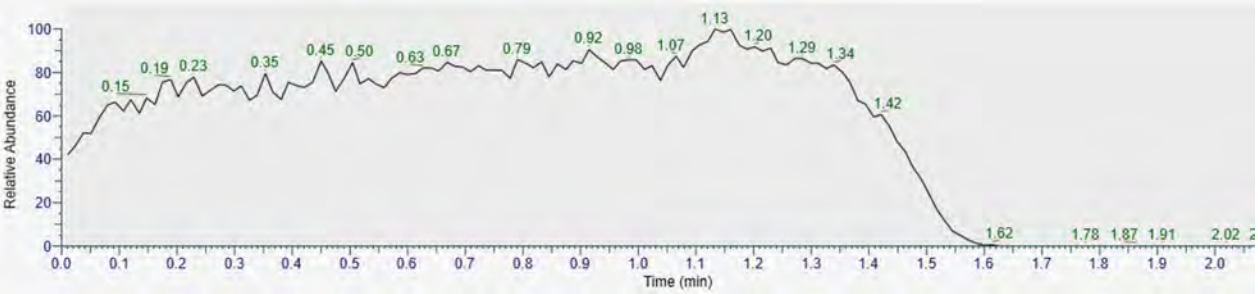

Figure 7.4 Example of spray duration observed using Whatman 1 paper with our custom designed μPAD at a tip angle of 15° and a pH of 2.0.

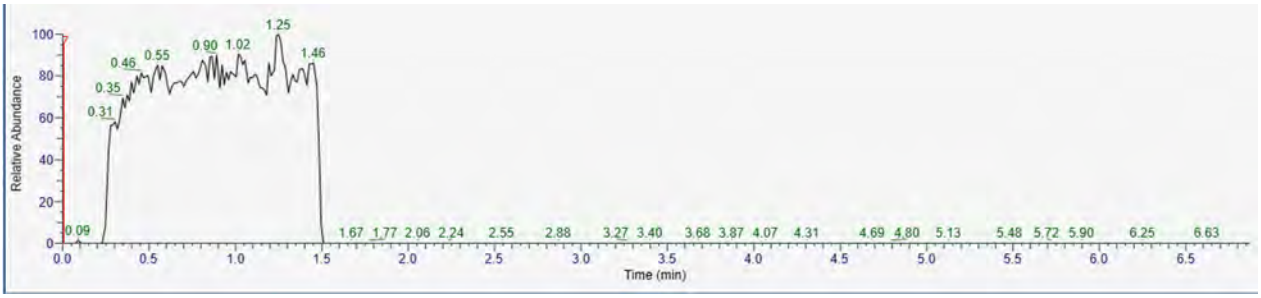

Figure 7.5 Example of spray duration observed using Whatman 1 paper with our custom designed μPAD at a tip angle of 45° and a pH of 3.3.

The normalized standard deviation values were 16.7% for Figure 7.3, 12% for Figure 7.4, and 10.4% for Figure 7.5. These percentages indicate a high degree of consistency in the ion signal during the PSI process.

Some variability between experiments can be attributed to differences in paper substrate, tip angle, pH conditions, and particularly the distance between the paper tip and the MS inlet. Although the exact position of the chip was not systematically recorded for each run, adjustments were made in real time to optimize signal stability, and the onset of myoglobin detection was used as a criterion for proper alignment (as visually confirmed by Dr. Hang via the Xcalibur live interface). Despite these expected variations, overall signal stability was consistently observed across all experiments. Furthermore, in most PS-MS measurements, the spray signal was maintained for approximately 1 to 2 minutes, providing a reliable acquisition window for spectral analysis.

Now that we have confirmed that our custom-designed μPADs enable the detection of protonated myoglobin across all tested parameter combinations, while providing a stable signal over time, we can proceed with the statistical analysis to draw conclusions on the character-

istics of PSI as a function of the different influencing parameters.

7.1.2 Statistical correlation of PSI performance with experimental parameters

When cross-correlating the Gaussian fitting parameters with the various PS-MS experimental conditions, the resulting Pearson correlation coefficients are summarized in the following Table 7.1.

Note 1: All Gaussian fitting parameters for each paper type at every considered pH condition are provided in Appendix C.

Note 2: Each experimental condition, defined by a unique combination of parameters, was performed only once ($n = 1$).

Table 7.1 Pearson correlation coefficients between physical variables (tip angle, pore size retention, flow rate ranking, and pH solvent) and Gaussian fitting parameters (A, μ, and σ) extracted from PS-MS spectra. Statistically significant correlations ($|r| > 0.5$) are shown in bold.

Variable	**Amplitude A**	**Center μ (z)**	**Width σ (z)**
Tip Angle	0.25	-0.01	0.17
Pore Size Retention	0.18	0.10	**-0.53**
Flow Rate	0.06	-0.01	0.21
pH	-0.27	**-0.82**	0.16

As shown in Table 7.1, the negative correlation between the solution pH and the Gaussian center μ indicates that μ increases as the pH decreases. This trend reflects the higher proton availability in more acidic conditions, enabling proteins to acquire additional fixed charges. As a result, ions tend to carry more charges on average, leading to the detection of higher charge states in the mass spectra.

Similarly, the negative correlation between pore size retention and the Gaussian width σ suggests that papers with smaller pore sizes favor broader charge state distributions.

To further investigate these relationships, the next section presents Pearson correlation analyses conducted under fixed pH conditions. This approach isolates the influence of paper-related variables (e.g., tip angle, pore size retention, ...) from chemical factors, enabling a clearer assessment of the correlation patterns. The effects of pH and other physicochemical properties will be examined separately in subsequent analyses.

7.1.3 PS-MS response at fixed solvent pH

In the following sections, each paper type was tested with all tip angle geometries under identical solvent conditions to evaluate their influence on PSI performance.

PS-MS signal response at pH=3.3

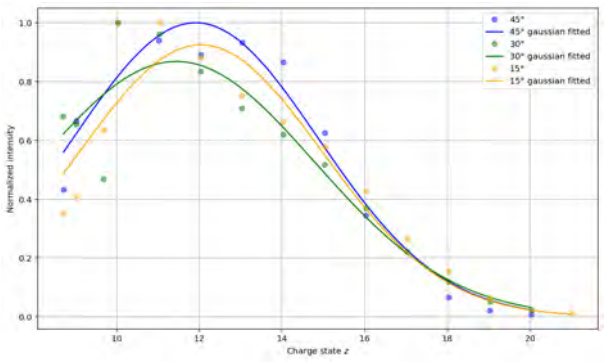

(a) Whatman 1

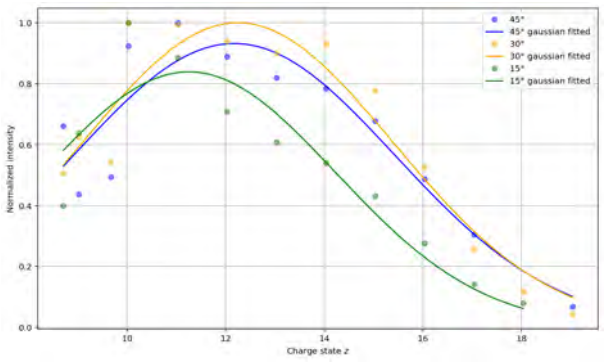

(b) Whatman 2

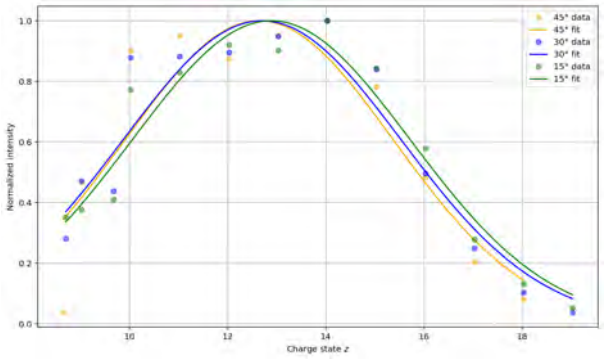

(c) Whatman 4

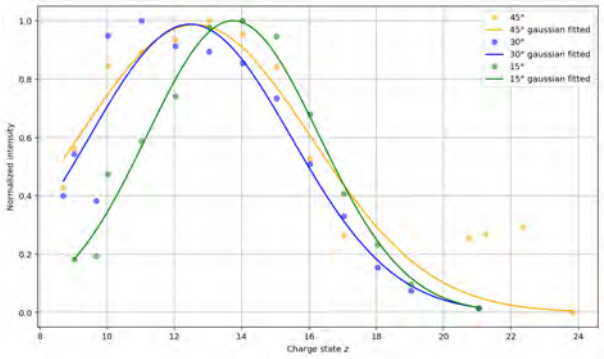

(d) Whatman 114

Figure 7.6 Relative abundance of myoglobin charge states (z) for the three tip angles (15°, 30°, 45°) for all the Whatman papers at pH=3.3.

Table 7.2 Pearson correlation coefficients between experimental parameters (tip angle, pore size retention, and flow rate ranking) and Gaussian fitting parameters (A, μ, and σ), based on mass spectra acquired for myoglobin in a 1:1 MeOH:H_2O solution with 0.1% acetic acid. Statistically significant correlations ($|r| > 0.5$) are shown in bold.

Parameter	**Amplitude A**	**Center μ (z)**	**Width σ (z)**
Tip Angle	0.30	-0.09	0.39
Pore Size Retention	**0.59**	**0.78**	-0.36
Flow rate	0.16	**0.515**	0.01

PS-MS signal response at pH=2.8

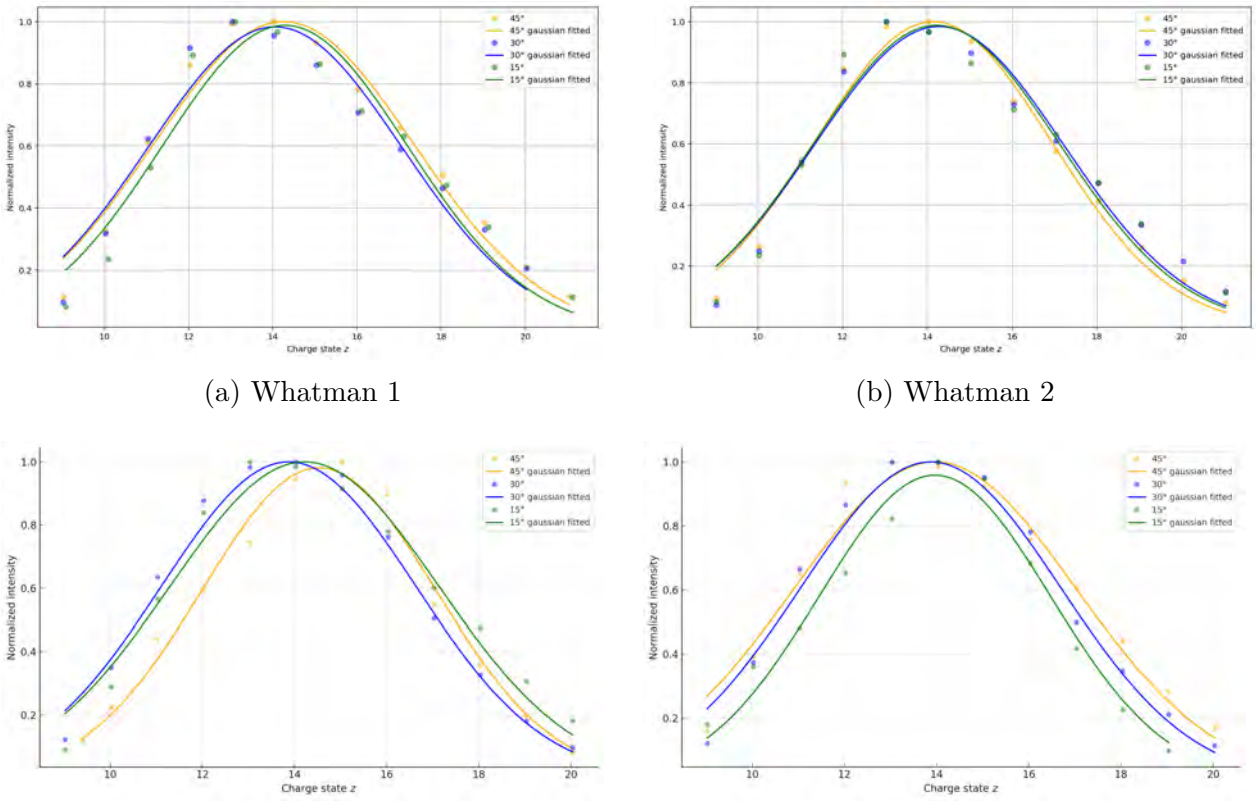

(a) Whatman 1

(b) Whatman 2

(c) Whatman 4

(d) Whatman 144

Figure 7.7 Relative abundance of myoglobin charge states (z) at three tip angles (15°, 30°, 45°) for different Whatman papers at pH=2.8

Table 7.3 Pearson correlation coefficients between experimental parameters (tip angle, pore size retention, and flow rate ranking) and Gaussian fitting parameters (A, μ, and σ), based on mass spectra acquired for myoglobin in a 1:1 MeOH:H_2O solution with 1% acetic acid. Statistically significant correlations ($|r| > 0.5$) are shown in bold.

Parameter	**Amplitude A**	**Center μ (z)**	**Width σ (z)**
Tip Angle	0.36	0.14	0.07
Pore Size Retention	0.25	-0.38	**-0.53**
Flow rate	0.04	-0.43	-0.04

PS-MS signal response at pH=2.0

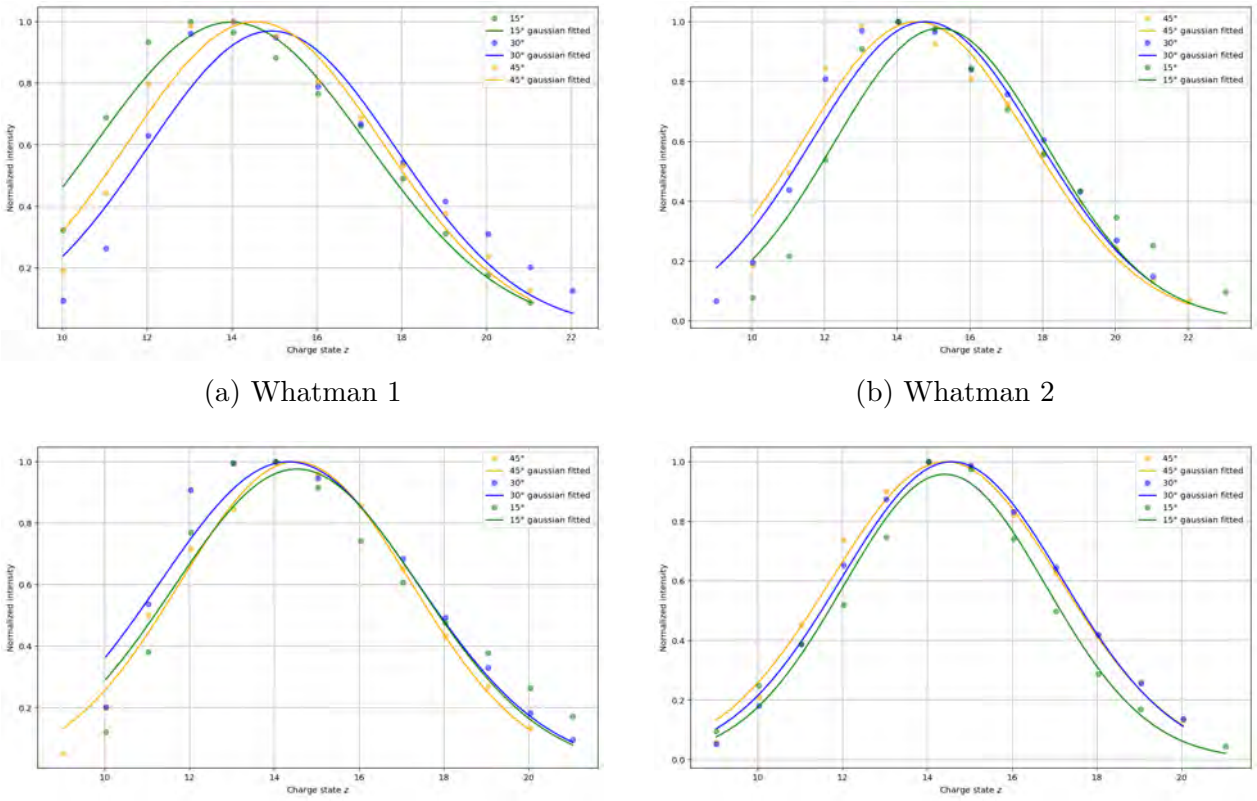

(a) Whatman 1

(b) Whatman 2

(c) Whatman 4

(d) Whatman 114

Figure 7.8 Relative abundance of myoglobin charge states (z) at three tip angles (15°, 30°, 45°) for different Whatman papers at pH=2.0.

Table 7.4 Pearson correlation coefficients between experimental parameters (tip angle, pore size retention, and flow rate ranking) and Gaussian fitting parameters (A, μ, and σ), based on mass spectra acquired for myoglobin in a 1:1 MeOH:H_2O solution with 3% acetic acid at pH = 2.0. Statistically significant correlations ($|r| > 0.5$) are shown in bold.

Parameter	**Amplitude** A	**Center** μ (z)	**Width** σ (z)
Tip Angle	0.22	-0.03	0.02
Pore Size Retention	-0.24	-0.38	**-0.80**
Flow rate	-0.36	-0.43	**-0.63**

7.1.4 General discussion and conclusion

Effect of pH = 3.3 on the spray signal

A robust positive correlation was found between pore retention size and both the Gaussian amplitude ($r = 0.59$) and the Gaussian center ($r = 0.78$). This indicates that larger pores promote the formation of bigger charged droplets, capable of sustaining higher charge states without disturbing evaporation kinetics. A positive correlation was also observed between the flow rate and the charge state center ($r = 0.51$). Although this correlation is weaker than that with pore size retention, it nonetheless shows that the flow rate contributes to modulating the charge state center of myoglobin. Moreover, the observed increase in signal amplitude as pore size retention increases demonstrates that analyte transmission remains uncompromised even with pore enlargement.

Effect of pH = 2.8 on the spray signal

Smaller pore retention sizes were correlated with broader charge-state distributions ($r = -0.53$). Under acidic conditions, droplets carry a high proton load, which increases the likelihood of multiple charging of myoglobin. Reduced pore sizes lead to the formation of smaller initial droplets with elevated surface-to-volume ratios, which in turn accelerate desolvation and limit both droplet coalescence and charge equilibration. Consequently, a wider distribution of charge states is observed.

Effect of pH = 2.0 on the spray signal

At this pH, both pore retention size and solvent flow rate exhibited a negative correlation with the Gaussian width. Smaller pores generate droplets with higher surface-to-volume ratios, which accelerate desolvation and concentrate charges, thereby broadening the ionization profile. Similarly, reduced solvent flow prolongs droplet residence time on the paper, allowing

more heterogeneous protonation of myoglobin and further widening the observed charge-state distribution.

Effect of pH on charge state distribution

Table 7.5 Pearson correlation coefficients between experimental parameters (tip angle and pH) and Gaussian fitting parameters (A, μ, and σ), based on mass spectra acquired for myoglobin using Whatman 1 paper-based.

Parameter	**Amplitude** A	**Center** μ (z)	**Width** σ (z)
Tip Angle (°)	0.373	0.050	-0.073
pH	**-0.454**	**-0.824**	0.053

Table 7.6 Pearson correlation coefficients between experimental parameters (tip angle and pH) and Gaussian fitting parameters (A, μ, and σ), based on mass spectra acquired for myoglobin using Whatman 2 paper-based.

Parameter	**Amplitude** A	**Center** μ (z)	**Width** σ (z)
Tip Angle (°)	0.223	0.020	0.331
pH	**-0.567**	**-0.876**	0.107

Table 7.7 Pearson correlation coefficients between experimental parameters (tip angle and pH) and Gaussian fitting parameters (A, μ, and σ), based on mass spectra acquired for myoglobin using Whatman 4 paper-based.

Parameter	**Amplitude** A	**Center** μ (z)	**Width** σ (z)
Tip Angle (°)	0.245	0.006	**-0.765**
pH	0.420	**-0.856**	-0.409

Table 7.8 Pearson correlation coefficients between experimental parameters (tip angle and pH) and Gaussian fitting parameters (A, μ, and σ), based on mass spectra acquired for myoglobin using Whatman 114 paper-based.

Parameter	**Amplitude** A	**Center** μ (z)	**Width** σ (z)
Tip Angle (°)	0.440	-0.202	**0.718**
pH	0.001	**-0.847**	**0.579**

For all paper types, a strong negative correlation was observed between pH and the charge state center (μ), with lower pH values consistently shifting the spectra toward higher charge

states, regardless of the paper's properties. This behavior reflects the increased protonation of myoglobin under acidic conditions. Figure 7.9 further illustrates this trend, showing that higher pH values shift the charge state distribution toward lower charges, following the same overall pattern across all tip angles.

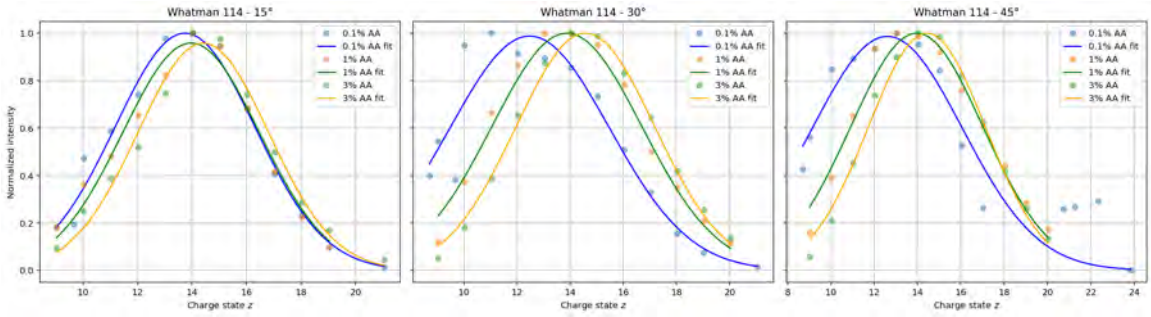

Figure 7.9 Example of mass spectra illustrating the effect of pH for Whatman 114 paper. These curves are extracted from the same dataset as used in the previous sections.

Note: While Whatman 114 is shown here as a representative example, a similar shift toward higher charge states with decreasing pH is consistently observed across all paper types.

Note: Even though each condition was tested only once ($n = 1$) due to technical constraints, the consistency of the trends observed across different pH values supports the reliability and interpretability of the results. This general pattern indicates that the findings remain meaningful and can be confidently discussed despite the limited number of replicates.

Beyond this common trend, each paper type exhibits specific behaviors. For instance, in the case of Whatman 1 and Whatman 2, lowering the pH results in an increase in signal amplitude. Both have the lowest pore size retention.

For Whatman 4, the tip angle strongly influenced the signal response, with a negative correlation between angle and the width (σ) of the charge-state distribution: smaller angles yielded broader distributions. In contrast, Whatman 114 showed the opposite trend, with broader charge distributions at larger tip angles and higher pH. This difference likely arises from intrinsic structural and wetting properties, as Whatman 114 exhibits a much higher flow rate than Whatman 4.

These results highlight the critical role of flow rate in electrospray ionization efficiency, consistent with previous literature. For Whatman 4, the relatively low flow rate limits mass transport to the tip, requiring a larger tip angle to homogenize ionization along the tip region. Conversely, Whatman 114, which is naturally more saturated due to its higher flow rate, behaves more similarly to the conditions used in the COMSOL model (see Chapter

6), where the substrate is already saturated. In this case, smaller tip angles enhance field localization and produce finer droplets; however, at high flow rates and limited proton availability, ionization becomes less equilibrated prior to droplet emission, resulting in broader charge state distributions.

Overall, tip angle, flow rate, and proton availability act synergistically to control droplet formation, charge transfer, and spectral response in PSI.

Moreover, the observed differences in charge state distributions can be interpreted by considering both the conformational state of myoglobin and the specific ionization mechanisms governing the PSI.

As described in Section 4.1.1, myoglobin predominantly exists in two main states:

- Holo form (heme-bound): Compact and globular, with buried basic residues, limiting protonation. Even under acidic conditions, this results in lower charge states.
- Apo form (heme-free): More unfolded, especially at low pH, exposing more protonation sites and leading to higher charge states.

These conformations influence ESI ionization models (see Chapter 2, Section 2.1.2):

- CRM: Droplets shrink until analytes retain residual charges—typical for folded proteins like holo-myoglobin, resulting in lower charge states.
- CEM: Unfolded proteins are ejected from droplets with high charges—consistent with apo-myoglobin, especially at low pH.

At low pH, denaturation favors apo-like behavior and CEM-type ionization, explaining the shift toward higher charge states. In contrast, near-neutral pH maintains compact structures, favoring CRM and resulting in lower center charge state .

CHAPTER 8 CONCLUSION

8.1 Summary of works

This work successfully addressed the three main objectives established for evaluating the PS-MS technique using custom-designed μPADs. It demonstrated the reliability of the device for protein detection under diverse experimental conditions, thereby confirming the robustness of the overall design.

This study provided new insights into the fundamental mechanisms governing PSI. By generating a stable and reproducible spray, the device enabled the consistent ionization of myoglobin, used here as a model protein, and allowed the detection of its distinct conformational states through the analysis of charge state distributions, encompassing both folded and unfolded forms. The results revealed that ionization efficiency and charge state distribution are strongly modulated by solution conditions and paper properties. At high pH, larger droplets promoted ionization, while the intrinsic properties of the paper—particularly the solvent flow rate—determined the charge state center of myoglobin. In contrast, at low pH, smaller droplets and reduced flow rates favored the formation of multiple protonation states. Moreover, pore size and solvent flow rate were found to be interdependent parameters that must be considered together when optimizing the tip angle. While previous studies have reported conflicting conclusions regarding the optimal tip geometry, our findings demonstrate that the tip angle cannot be optimized in isolation, but rather depends on the combined effects of pore size and flow rate. Taken together, these findings highlight the strong interplay between paper architecture, device geometry, and solution conditions in shaping droplet formation, ionization, and charge transfer in PS-MS.

The physico-chemical properties and functional behavior of the paper substrates were investigated through a combination of experimental characterization and model-based interpretation. Capillary flow experiments, analyzed using the Lucas–Washburn model, demonstrated the influence of pore size and paper thickness on solvent transport and solvent–substrate interactions. ESEM imaging provided insight into structural features such as pore architecture and surface morphology, while also revealing laser-cutting artifacts including edge degradation and localized structural alterations. However, laser-cut fabrication proved highly reproducible and scalable, allowing the efficient production of multiple low-cost devices. Finally, COMSOL simulations provided complementary insight into the electrostatic field distributions near the paper tip. The results showed that smaller tip angles generate stronger and more confined electric fields favoring localized ionization at higher flow rates. Such

simulation-guided approaches not only deepen the physical understanding of PSI, but also advance the technique beyond empirical optimization toward theory-guided design. From a technological perspective, the integration of this methodology with portable mass spectrometry enables user-friendly, environmentally sustainable, and field-deployable solutions, which are particularly valuable for point-of-care diagnostics.

Overall, this work demonstrates that our chip enables robust and reproducible protein detection via PS-MS, while providing a versatile platform to investigate how geometry, material properties, and solution chemistry govern ionization efficiency. To the best of our knowledge, this represents the first paper-based lab-on-a-chip device that enhances PS-MS analyses through the integration of microfluidics and laser cutting. In addition, this study highlights the potential of paper chips for high mass resolution analysis. The pronounced sensitivity of PSI to substrate microstructure, tip angle, and protein conformation underscores the importance of combining experiments and simulations for the rational optimization of μPADs. Together, these findings establish a foundation for improving performance and expanding the analytical applications of porous substrates in biomolecular analysis.

8.2 Limitations

While the proposed μPADs platform demonstrated stable ionization and reliable protein detection, several limitations remain:

- Material-related constraints: Due to manufacturing limitations of Whatman papers, it was not possible to investigate thickness and porosity separately.
- Operational variability: Maintaining identical experimental conditions, particularly the tip-to-MS inlet distance and the spray mode, proved challenging. Real-time adjustments were often required to achieve stable single-jet operation, introducing variability in ionization efficiency across experiments.
- Laser cutting artifacts: The fabrication of μPADs using laser cutting introduced edge irregularities and localized structural damage. These artifacts may vary between batches, potentially impacting reproducibility.
- Spray observation: Direct observation of the spray could have provided additional insights; however, this was not feasible due to equipment limitations.
- Statistical limitations: Increasing the statistical power in the PS-MS experiments would have been beneficial, as certain parameter combinations were tested only once, limiting the robustness of the conclusions.

These limitations underline the need for improved fabrication protocols, more precise geometric control, environmental stabilization, and standardized operational procedures. Addressing these aspects would enhance reproducibility.

8.3 Future Research

Future developments of the μPAD should focus on expanding the analytical framework and improving fabrication precision.

- Incorporating a fixed positioning system to precisely control the tip-to-MS inlet distance would minimize geometric variability and promote more stable spray performance.
- Enhancing the reproducibility of laser cutting, for instance by refining cutting parameters or integrating structural supports to stabilize the paper during processing, would reduce edge irregularities and preserve substrate integrity across different batches.
- Further investigations of the COMSOL simulation could be made in order to visualize the droplet formation for the different substrate geometry across various solvent for the different MS-inlet distance in all axial directions.

Collectively, these improvements would increase the robustness of the technique and enable more systematic investigations into the relationship between material properties, device design, and operational parameters governing PS-MS performance.

REFERENCES

[1] A. Voda, R. Mareš, and Z. Sedláková, *Viscosities and densities of methanol + water mixtures at 25°C.* Elsevier, 2003, fluid Phase Equilibria, Vol. 210, pp. 143–150.

[2] S. Hovorka and Z. Sedláková, *Densities of binary mixtures of methanol and water.* Elsevier, 1998, fluid Phase Equilibria, Vol. 145, pp. 123–132.

[3] R. Pashley *et al.*, *Decreased evaporation rate of water in confined geometries.* American Chemical Society, 2005, the Journal of Physical Chemistry B, Vol. 109, pp. 1231–1238.

[4] A. Rodríguez *et al.*, *Surface tension of binary mixtures of methanol and water with acetic acid at 25°C.* Elsevier, 2010, journal of Colloid and Interface Science, Vol. 345, pp. 402–408.

[5] J. Wang *et al.*, *Wettability of filter paper with aqueous and organic liquids.* American Chemical Society, 2009, langmuir, Vol. 25, pp. 7442–7446.

[6] S. Banerjee and S. Mazumdar, *Electrospray Ionization Mass Spectrometry: A Technique to Access the Information beyond the Molecular Weight of the Analyte.* Hindawi Publishing Corporation: International Journal of Analytical Chemistry, 2012, dOI: 10.1155/2012/282574.

[7] B. M. Cummins *et al.*, *Time-Dependent Model for Fluid Flow in Porous Materials with Multiple Pore Sizes.* Analytical Chemistry, 92(17), 11933–11941, 2020, technical Note, American Chemical Society.

[8] R. D. Espy *et al.*, *Spray mechanism in paper spray ionization.* Elsevier, 2012, international Journal of Mass Spectrometry, available online 6 July 2012.

[9] T. M. H. Nguyen, W.-Y. Song, and T.-Y. Kim, *Characterization of spray modes and factors affecting the ionization efficiency of paper spray ionization.* MDPI, 2021, micromachines, Vol. 12, No. 3, 303, doi:10.3390/mi12030303.

[10] Q. Yang *et al.*, *Paper spray ionization devices for direct, biomedical analysis using mass spectrometry.* Elsevier, 2012, international Journal of Mass Spectrometry, Vol. 312, pp. 201–207, doi:10.1016/j.ijms.2011.05.013.

[11] D. W. Woodall *et al.*, *Understanding the Thermal Denaturation of Myoglobin with IMS-MS: Evidence for Multiple Stable Structures and Trapped Pre-equilibrium States.*

Journal of the American Society for Mass Spectrometry, 2021, vol. 32, research Article. [Online]. Available: https://pubs.acs.org/doi/10.1021/jasms.0c00380

[12] A. Zhang *et al.*, *Modern analytical techniques in metabolomics analysis.* Analyst, 137, 293: Royal Society of Chemistry, 2012, dOI: 10.1039/c1an15605e.

[13] J. Liu *et al.*, *Development, Characterization, and Application of Paper Spray Ionization.* American Chemical Society, 2010, analytical Chemistry, Vol. 82, No. 6, pp. 2463–2471, doi:10.1021/ac100045q.

[14] B. S. Frey, D. E. Damon, and A. K. Badu-Tawiah, *Emerging trends in paper spray mass spectrometry: Microsampling, storage, direct analysis and applications.* Wiley, 2020, mass Spectrometry Reviews, Vol. 39, No. 4, pp. 336–370, doi:10.1002/mas.21601.

[15] S. J. An *et al.*, *Simple Protein Analysis by Droplet Paper Spray Ionization Mass Spectrometry with Polyolefin Silica-Based Paper.* Basel, Switzerland: MDPI, 2022, originally published in the journal *Molecules*, Volume 27, Issue 15, Article 4950. [Online]. Available: https://www.mdpi.com/1420-3049/27/15/4950

[16] Y. Ren *et al.*, *Analysis of Biological Samples Using Paper Spray Mass Spectrometry: An Investigation of Impacts by the Substrates, Solvents and Elution Methods.* Chromatographia, 76:1339–1346: Springer-Verlag, 2013, dOI: 10.1007/s10337-013-2458-y.

[17] S. Vadakedath *et al.*, *The Principle, Types, and Applications of Mass Spectrometry: A Comprehensive Review.* Science and Education Publishing, 2022, published in Biomedicine and Biotechnology, Vol. 7, No. 1, pp. 6–22. [Online]. Available: https://doi.org/10.12691/bb-7-1-2

[18] F.-Y. Che, H.-T. Deng, and S.-J. Ding, *Mass Spectrometry Applications in Biomedical Research.* BioMed Research International, Volume 2015, Article ID 827370: Hindawi Publishing Corporation, 2015, editorial, Open access under CC BY 3.0. [Online]. Available: http://dx.doi.org/10.1155/2015/827370

[19] M.-Z. Huang *et al.*, *Ambient Ionization Mass Spectrometry: A Tutorial.* Analytica Chimica Acta, Volume 702, Pages 1–15: Elsevier, 2011, available online 22 June 2011.

[20] J. B. Fenn *et al.*, *Electrospray ionization for mass spectrometry of large biomolecules.* AAAS, 1989, science, Vol. 246, No. 4926, pp. 64–71, doi:10.1126/science.2675315.

[21] S. Banerjee and S. Mazumdar, *Electrospray Ionization Mass Spectrometry: A Technique to Access the Information beyond the Molecular Weight of the Analyte.* London, UK:

Hindawi Publishing Corporation, 2012, originally published in the International Journal of Analytical Chemistry, DOI: 10.1155/2012/282574.

[22] G. I. Taylor, *Disintegration of Water Drops in an Electric Field*. Proceedings of the Royal Society of London. Series A, Mathematical and Physical Sciences, 1964, vol. 280, no. 1382, original scientific article.

[23] M. Karas and R. Krüger, *Ion formation in MALDI: The cluster ionization mechanism*. American Chemical Society, 2003, chemical Reviews, Vol. 103, No. 2, pp. 427–439, doi:10.1021/cr010376c.

[24] D. Abrahamsson *et al.*, *Modeling the Relative Response Factor of Small Molecules in Positive Electrospray Ionization*. RSC Advances, Volume 14, Pages 37470–37482: Royal Society of Chemistry, 2024, open Access article licensed under CC BY-NC 3.0. [Online]. Available: https://doi.org/10.1039/D4RA06695B

[25] A. K. Yetisen, M. S. Akram, and C. R. Lowe, *Paper-based microfluidic point-of-care diagnostic devices*. Royal Society of Chemistry, 2013, lab on a Chip, Vol. 13, No. 12, pp. 2210–2251.

[26] G. M. Whitesides *et al.*, *Patterned Paper as a Platform for Inexpensive, Low-Volume, Portable Bioassays*. Angewandte Chemie International Edition, 2007, vol. 46, no. 8, originally published as a scientific article, reformatted here as a reference book entry for citation consistency.

[27] A. W. Martinez *et al.*, *Simple telemedicine for developing regions: camera phones and paper-based microfluidic devices for real-time, off-site diagnosis*. American Chemical Society, 2007, analytical Chemistry, Vol. 79, No. 14, pp. 5294–5300.

[28] A. Manz, N. Graber, and H. M. Widmer, *Miniaturized Total Chemical Analysis Systems: A Novel Concept for Chemical Sensing*. Amsterdam: Elsevier, 1990, originally published in *Sensors and Actuators B: Chemical*, Vol. 1, Issues 1–6, pp. 244–248.

[29] S. Nishat *et al.*, *Paper-based Microfluidics: Simplified Fabrication and Assay Methods*. Sensors and Actuators B: Chemical, 2021, vol. 336, elsevier.

[30] R. J. Roberts and D. R. Woods, *Wicking in porous materials: Nonuniform liquid penetration into paper*. AIChE Journal, Vol. 49, No. 10, pp. 2637–2645, 2003, originally published as a journal article.

[31] H. Wang *et al.*, *Paper spray for direct analysis of complex mixtures using mass spectrometry.* American Chemical Society, 2010, analytical Chemistry, Vol. 82, No. 6, pp. 2463–2471.

[32] M. S. Wilm and M. Mann, *Electrospray and Taylor-Cone theory, Dole's beam of macromolecules at last?* Elsevier, 1994, international Journal of Mass Spectrometry and Ion Processes, Vol. 136, pp. 167–180, doi:10.1016/0168-1176(94)85008-5.

[33] G. Huang *et al.*, *Corona discharge in the ionization of compounds using paper spray mass spectrometry.* Springer, 2015, journal of the American Society for Mass Spectrometry, Vol. 26, No. 2, pp. 279–286, doi:10.1007/s13361-014-1004-7.

[34] G. W. Vandergrift *et al.*, *Paper Spray Mass Spectrometry for the Direct, Semi-Quantitative Measurement of Fentanyl and Norfentanyl in Complex Matrices.* Elsevier, 2018, published in *Clinical Biochemistry*, Volume 54, Pages 106–111.

[35] D. E. Damon *et al.*, "Determining surface energy of porous substrates by spray ionization," *Langmuir*, vol. 35, no. 41, pp. 13 853–13 859, 2019.

[36] P. Nemes, I. Marginean, and A. Vertes, *Spraying mode effect on droplet formation and ion chemistry in electrosprays.* American Chemical Society, 2007, analytical Chemistry, Vol. 79, No. 8, pp. 3105–3116, doi:10.1021/ac062200x.

[37] Y. Su *et al.*, *Quantitative paper spray mass spectrometry analysis of drugs of abuse.* Royal Society of Chemistry, 2013, analyst, Vol. 138, No. 15, pp. 4443–4447, doi:10.1039/c3an00934c.

[38] Y. Ueda *et al.*, *Simple Protein Analysis by Droplet Paper Spray Ionization Mass Spectrometry.* MDPI, 2023, molecules, Vol. 28, No. 21, Article 7339, doi:10.3390/molecules28217339.

[39] M. Girod *et al.*, *Effect of solvent composition on chemical equilibrium and ionization efficiency in paper spray mass spectrometry.* Royal Society of Chemistry, 2011, the Analyst, Vol. 136, No. 24, pp. 5031–5036.

[40] Y. Zhu *et al.*, *Fundamental study of the spray mechanism in paper spray mass spectrometry using fast photography.* Royal Society of Chemistry, 2013, analyst, Vol. 138, pp. 3548–3554.

[41] B. J. Bills *et al.*, *Influence of paper geometry on paper spray ionization.* Royal Society of Chemistry, 2018, analyst, Vol. 143, pp. 3974–3982.

[42] T. Wang *et al.*, *Sub-ppt Mass Spectrometric Detection of Therapeutic Drugs in Complex Biological Matrixes Using Polystyrene-Microsphere-Coated Paper Spray.* Washington, DC: Analytical Chemistry, American Chemical Society, 2017, originally published in *Analytical Chemistry*, 89(12), 2017, pp. 6431–6436. DOI: https://doi.org/10.1021/acs.analchem.7b00378.

[43] J. Ji *et al.*, *Ambient Ionization Based on Mesoporous Graphene Coated Paper for Therapeutic Drug Monitoring.* Amsterdam: Journal of Chromatography B, Elsevier, 2016, originally published as a journal article: J. Chromatogr. B 1015–1016 (2016): 45–52. DOI: https://doi.org/10.1016/j.jchromb.2016.01.040.

[44] X. Li, P. Zwanenburg, and X. Liu, "Design of paper-based microfluidic devices for electrochemical sensing of heavy metal ions," *Lab on a Chip*, vol. 15, pp. 2826–2833, 2015.

[45] D. Gao and et al., "Design of 3d paper-based microfluidic devices for chemical analysis," *Biosens. Bioelectron.*, vol. 81, pp. 415–421, 2016.

[46] S. Chiang, W. Zhang, and Z. Ouyang, *Paper spray ionization mass spectrometry: recent advances and clinical applications.* Taylor & Francis, 2018, expert Review of Proteomics, Vol. 15, No. 10, pp. 781–789, doi:10.1080/14789450.2018.1525295.

[47] H. Wang *et al.*, *Direct analysis of biological tissue by paper spray mass spectrometry.* American Chemical Society, 2010, analytical Chemistry, Vol. 82, No. 6, pp. 2262–2267, doi:10.1021/ac902918c.

[48] Q. Yang *et al.*, *Wax-Printed Paper Substrates for Paper Spray Mass Spectrometry.* Analytical Chemistry (ACS Publications), 2016, originally published as a journal article in *Analytical Chemistry*, Vol. 88, No. 7, pp. 3824–3830. DOI: 10.1021/acs.analchem.5b04546.

[49] H. Wang *et al.*, *Three-Dimensional Cartridge Configuration for Paper Spray Mass Spectrometry.* Analytical Chemistry (ACS Publications), 2017, originally published as a journal article in *Analytical Chemistry*, Vol. 89, No. 21, pp. 11779–11785. DOI: 10.1021/acs.analchem.7b03228.

[50] X. Wang, E. R. Williams, and D. Raftery, *Ambient Ionization Mass Spectrometry for Point-of-Care Diagnostics and Other Clinical Applications.* Volume 62, Issue 1, Pages 4–12: Clinical Chemistry, 2016, originally published as journal article. DOI: 10.1373/clinchem.2015.240846.

[51] RCSB Protein Data Bank, *RCSB PDB: Protein Data Bank*. https://www.rcsb.org: RCSB PDB Foundation, 2025, accessed July 20, 2025.

[52] ChemicalBook, *Crystal Violet – Product Properties*. Online resource: ChemicalBook, 2025, available at: https://www.chemicalbook.com/ChemicalProductProperty_EN_CB2161846.htm (Accessed: 2025-07-23).

[53] N. Koursari *et al.*, *Drying of Foam under Microgravity Conditions*. Cham: Springer, 2019, microgravity Science and Technology, Vol. 31, pp. 589–601.

APPENDIX A PHYSICOCHEMICAL PARAMETERS USED FOR COMSOL MODELING

Table A.1 Comparison of estimated physical properties of 1:1 methanol–water mixtures containing acetic acid, used in COMSOL simulations. Values are based on experimental or interpolated data from [1–5].

Property	**Symbol**	**No AA**	**0.1% AA**	**1% AA**	**3% AA**
Relative permittivity	ε_r	55	55	52–54	50–52
Dynamic viscosity (Pa·s)	μ	1.534×10^{-3}	$\sim 1.53 \times 10^{-3}$	$\sim 1.55 \times 10^{-3}$	1.6×10^{-3}
Density (kg/m^3)	ρ	910–915	915	920–925	930–935
Electrical conductivity (S/m)	σ	~ 1–2×10^{-4}	$\sim 3.5 \times 10^{-4}$	$\sim 1.5 \times 10^{-3}$	3.0×10^{-3}
Surface tension (N/m)	γ	~ 0.040	~ 0.038	0.033–0.035	0.031–0.033
Contact angle (°)	θ	45–50	35–45	30–40	25–35

APPENDIX B PRELIMINARY WORK

Prototype development strategy

To achieve the current paper-based chip geometry, my colleague Sabrina Zoso developed several prototypes through an iterative approach. While we do not detail each design stage, we present the experimental rationale behind the final configuration. Rather than relying on theoretical models, the design was guided by experiments showing improved signal stability and intensity in PS-MS. Each iteration helped refine signal quality, mechanical stability, and MS compatibility, with successive prototypes addressing specific limitations.

Prior works and geometry optimization

Throughout the development of the paper-based chip, various parameters were systematically tested, including paper type and thickness, probe geometry (width, length, angle), presence of a solution chamber, and conductive material integration.

Tested designs and parameters

Initial experiments focused on triangular cutouts with varying base widths (20–40 mm) and angles (22.5°, 45°, 90°) on Whatman 1 filter paper. Subsequently, a solution chamber was introduced to isolate the sample zone from the base and prevent backflow. Designs were further modified with widened tips for improved flow, reinforced edges, and structural supports such as Polyméthacrylate de Méthyle (PMMA) frames. Different conductive strategies were explored, including graphite coatings, Ag-epoxy, copper wires, and tape, as well as treatments like ethanol soaking, sonication, and thermal purification.

Outcomes and limitations

The 20 mm width with a 45° angle consistently offered the best signal stability (1 to 2 minutes). Larger probes deformed more easily, while sharper angles (e.g., 22.5°) caused flow irregularities. Graphite, while conductive, introduced significant background noise and dissolved in ethanol. Ag-epoxy introduced interference in the lipid region, while carbon nanotubes (CNTs) proved challenging to apply in a consistent and reproducible manner. Paper deformation and solution leakage were recurrent issues, particularly when using thinner paper or poorly sealed chambers — in some cases, the laser-cut holes were too thin, allowing

liquid to seep through the walls. Structural reinforcements and channel widening improved flow but did not fully resolve reproducibility issues.

Optimized geometry

The current design uses reinforced Whatman 114 paper with a 20 mm base and 45° tip, to avoid tip bending and a solution chamber for flow control. Copper tape proved to be the most reliable conductive material, minimizing background signals. Soaking and localized sonication with pure water reduced persistent background peaks, and laser-cutting contamination was mitigated by spatial repositioning. The final design balances mechanical stability, signal clarity, and reproducibility, and serves as the optimized platform for downstream analytical applications.

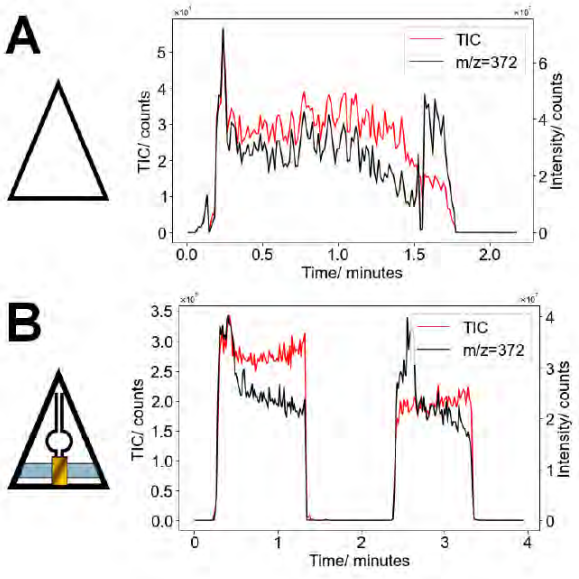

Figure B.1 Total ion count (TIC, red) and CV signal intensity at m/z = 372 (black) as a function of time, comparing the standard triangular paper (20 × 30 mm) and the proposed paper-based microfluidic device.

As shown in Figure B.1, the designed chip provides improved stability. The resulting signal exhibits a rectangular-like shape, indicating consistent and sustained ion emission. Previous approaches relied on costly photolithography equipment and cleanroom environments to pattern paper-based devices. In contrast, the improved method presented here uses laser cutting to fabricate paper-based chips with controlled microfluidic features. To the best of our knowledge, this is the first paper-based microfluidic device specifically designed to enhance PS-MS analyses. The first characterization of this paper-based chip was performed using the

chemical compound crystal violet (CV).

Note: CV was selected as a model compound due to its strong ionization efficiency in positive mode, chemical stability, and well-defined signal at m/z = 372. Its intense color also facilitates visual tracking within the microfluidic device. These properties make CV an ideal standard for evaluating the performance and reproducibility of paper-based PS-MS systems.

The improved high voltage found applied was 3.5 kV, using a methanol:water solvent mixture at 1% v/v, with aliquot volumes of 20 μL.

Calibration Strategy

The detectability of [CV] was confirmed and following the optimization of the paper device geometry, a two-part calibration strategy was developed to ensure reliable and reproducible performance of the PSI system.

The first step assessed the relationship between analyte concentration and signal intensity under fixed solvent conditions (1:1 methanol–water). A series of CV solutions ranging from 0.01 to 10 µM was used to generate a concentration-response curve. This allowed evaluation of the system's linear range, detection and quantification limits, and served as a reference for comparing results across various geometries and spray conditions.

The second step focused on the effect of solvent composition. Using a fixed CV concentration (5 µM), the methanol–water ratio was varied from 100% water to 100% methanol. This aimed to quantify how solvent properties (e.g., polarity, volatility, conductivity) affect ionization efficiency and spray stability. Relative Ionization Efficiency Factors (RIEFs) were derived to correct for solvent-induced signal variation. The study also sought to identify the optimal solvent mixture that balances analyte solubility and spray duration. Together, these two steps provide a complete framework for understanding and controlling key variables in PSI, enabling accurate quantitative analysis even under complex or variable experimental conditions.

Crystal Violet Calibration Protocol

To construct the calibration curve, CV solutions (0.01 to 10 µM) were spotted in equal volumes on triangular paper substrates and air-dried. Samples were analyzed using an LTQ Orbitrap Velos mass spectrometer at a constant spray voltage of 3.25 kV.

For each sample, the four strongest time points in the total ion chromatogram (TIC) were selected, and their corresponding full-scan spectra were extracted. The signal intensity at

$m/z = 372$ (CV ion) was averaged across the four spectra to represent that concentration.

The resulting calibration curve plotted CV concentration versus average signal intensity. Standard deviation (SD) and standard error of the mean (SEM) were calculated to assess signal stability. Signal-to-noise ratios (S/N) were used to determine the limits of detection (LOD, S/N = 3) , providing a robust evaluation of the PS-MS system's quantitative sensitivity for CV.

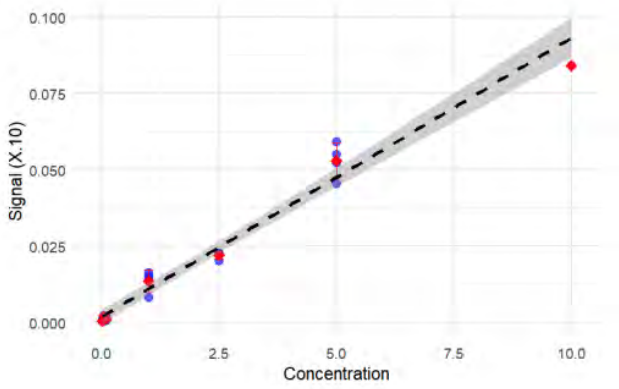

Figure B.2 Calibration curve using crystal violet (CV) concentrations of 0.1 µM, 1.0 µM, 2.5 µM, 5 µM, and 10 µM, applied on the designed paper device with a volume of 20 µL.

APPENDIX C GAUSSIAN FIT PARAMETERS FOR DIFFERENT WHATMAN PAPERS, TIP ANGLES, AND PH SOLVENT

Table C.1 Gaussian fit parameters for various Whatman paper types under different tip angles and solvent pH conditions.

Paper Type	**Tip Angle (°)**	**Amplitude A**	**Center μ (z)**	**Width σ (z)**	**pH**
Whatman 1	15	0.9248	12.0346	2.9405	3.3
Whatman 1	30	0.8683	11.4397	3.3473	3.3
Whatman 1	45	1.0179	11.9142	2.9264	3.3
Whatman 1	15	0.9882	14.29	2.91	2.8
Whatman 1	30	0.9833	14.05	3.01	2.8
Whatman 1	45	1.010	14.30	3.06	2.8
Whatman 1	15	0.999	13.98	3.20	2.0
Whatman 1	30	0.970	14.93	2.94	2.0
Whatman 1	45	1.010	14.55	2.99	2.0
Whatman 2	15	0.8388	11.2522	2.9728	3.3
Whatman 2	30	1.0288	12.2610	3.0800	3.3
Whatman 2	45	0.9318	12.1714	3.2590	3.3
Whatman 2	15	0.9882	14.21	2.91	2.8
Whatman 2	30	0.9843	14.27	2.94	2.8
Whatman 2	45	1.020	14.10	2.76	2.8
Whatman 2	15	0.9777	15.16	2.91	2.0
Whatman 2	30	1.200	14.80	3.09	2.0
Whatman 2	45	1.000	14.54	3.11	2.0
Whatman 4	15	1.017	12.8903	2.8047	3.3
Whatman 4	30	1.039	12.71	2.7621	3.3
Whatman 4	45	1.0603	12.64	2.6324	3.3
Whatman 4	15	1.0094	14.2144	2.8960	2.8
Whatman 4	30	1.0446	13.8709	2.6778	2.8
Whatman 4	45	0.9811	14.53	2.53	2.8
Whatman 4	15	0.9761	14.53	2.90	2.0
Whatman 4	30	1.040	14.44	2.94	2.0
Whatman 4	45	1.010	14.50	2.71	2.0
Whatman 114	15	1.020	13.70	2.5300	3.3
Whatman 114	30	0.9880	12.4708	3.0083	3.3
Whatman 114	45	0.9866	12.6024	3.4702	3.3
Whatman 114	15	0.9584	13.96	2.5100	2.8
Whatman 114	30	1.0400	13.90	2.7400	2.8
Whatman 114	45	1.0200	14.00	3.0000	2.8
Whatman 114	15	0.9579	14.41	2.4000	2.0
Whatman 114	30	1.0200	14.60	2.5800	2.0
Whatman 114	45	1.0200	14.40	2.6500	2.0